# An 8 × 8 MIMO Radar System Utilizing Cascadable Transceiver MMICs With On-Chip Antennas at 240 GHz

Jonathan Bott, *Graduate Student Member, IEEE*, Muhammed Ali Yildirim, *Graduate Student Member, IEEE*, Benedikt Sievert, *Member, IEEE*, Florian Vogelsang, *Graduate Student Member, IEEE*, Tobias Welling, Philipp Konze, Daniel Erni, *Member, IEEE*, Andreas Rennings, *Member, IEEE*, and Nils Pohl, *Senior Member, IEEE*

***Abstract*— This article introduces a 240-GHz multiple-input–multiple-output (MIMO) radar chipset, consisting of a 120-GHz voltage-controlled oscillator (VCO) monolithic microwave integrated circuit (MMIC) for generating the local oscillator (LO) signal and a 240-GHz transceiver (TRX) MMIC, doubling the frequency and containing one transmitter (Tx) and one receiver (Rx) channel. The Tx channel has a digital vector modulator (VM), allowing for phase adjustments. The 120-GHz VCO has a tuning range of 27.2 GHz (23.6%). The MIMO frequency-modulated continuous-wave (FMCW) system capabilities are demonstrated using a phase-locked loop (PLL)-based VCO stabilization generating wideband, 30-GHz FMCW chirps, which are radiated using a time-division multiplexing (TDM) technique. The MMICs feature a cascadable approach, enabling the scalability of the array size by placing multiple TRX MMICs close to each other using a daisy chain approach. Furthermore, a circular polarized on-chip antenna allows rotation of the MMICs, and the TRX MMIC can be connected to two adjacent edges of the VCO MMIC, creating a 2D array for detecting targets in 3-D space. In the demonstrator setup using eight MMICs, the eight Tx channels of the MMICs generate an equivalent isotropically radiated power (EIRP) of 0 dBm each, reflected from the target and received by eight Rx channels. Overall, the demonstrator system contains 64 virtual elements integrated on an array size of less than 10 × 10 mm$^2$.**

***Index Terms*— B11HFC, bipolar complementary metal-oxide-semiconductor (BiCMOS), circular polarization, Colpitts oscillator, *D*-band, frequency divider, frequency doubler, frequency multiplier, frequency-modulated continuous wave (FMCW), Gilbert cell, industrial, scientific and medical (ISM) band, Infineon Technology AG, *J*-band, millimeter-wave (mm-wave) technology, mixer, multiple-input–multiple-output (MIMO), on-chip antenna, power amplifier (PA), radar, receiver (Rx), silicon–germanium (SiGe), system-on-chip (SoC), time-division multiplexing (TDM), transmitter (Tx), vector modulator (VM), voltage-controlled oscillator (VCO), wideband, Wilkinson (WK) power divider, WR-43, WR-80.**

## I. Introduction

MULTIPLE-INPUT–MULTIPLE-OUTPUT (MIMO) radar systems play a crucial role in various aspects of daily life. They are improving driving assistance systems in vehicles [1], [2], [3], making hidden objects visible in security scanners [4], [5], [6], [7], [8], and improving industrial processes through nondestructive testing [9], [10]. While the 61-GHz industrial, scientific and medical (ISM) band and the 77-GHz automotive band were established commercially over a decade ago [2], silicon-based 122-GHz ISM applications are still emerging, and radar research primarily targets higher millimeter-wave (mm-wave) or sub-terahertz (THz) frequencies.

The development toward higher frequencies in radar systems is motivated by the increased bandwidth needed for target differentiation [2], [11, p. 8] and by building more compact systems or increasing the channel count using the same form factor. Consequently, research into silicon–germanium (SiGe)-based THz circuits has been ongoing for approximately a decade [12], [13], [14], [15]. While the design of silicon-based THz systems presents significant challenges, the advantages of operating at higher frequencies extend beyond bandwidth enhancement and include material detection and classification capabilities in various industrial, medical, and security applications [16], [17], [18], [19], [20], [21], [22], [23].

While 77- and 122-GHz radar systems predominantly rely on RF substrates for routing the transmitter (Tx) and receiver

Manuscript received 16 May 2024; revised 26 July 2024; accepted 28 August 2024. Date of publication 3 September 2024; date of current version 18 September 2024. This work was supported in part by German Research Foundation ("Deutsche Forschungsgemeinschaft," DFG) under Project 287022738 (TRR 196 for Projects C02, C03, and C05), in part by German Ministry for Economic Affairs and Climate Action [Bundesministerium für Wirtschaft und Klimaschutz (BMWK)] through the URBANSens Project within the Research Program LuFo VI-2 under Grant 20D2106B, in part by German Federal Ministry of Education and Research [Bundesministerium für Bildung und Forschung (BMBF)] in the Course of the 6GEM Research Hub under Grant 16KISK037, and in part by the Ministry of Culture and Science of the Federal State of North-Rhine-Westphalia in the Framework of "Netzwerke 2021" as part of the Project "terahertz.NRW" under Project NW21-068D. *(Corresponding author: Jonathan Bott.)*

Jonathan Bott, Muhammed Ali Yildirim, Florian Vogelsang, Tobias Welling, and Philipp Konze are with the Institute of Integrated Systems, Ruhr University Bochum, 44801 Bochum, Germany (e-mail: jonathan.bott@rub.de).

Benedikt Sievert is with the Fraunhofer Institute for High Frequency Physics and Radar Techniques (FHR), 53343 Wachtberg, Germany.

Daniel Erni and Andreas Rennings are with the Laboratory for General and Theoretical Electrical Engineering (ATE), Faculty of Engineering, and the Center for Nanointegration Duisburg-Essen (CENIDE), University of Duisburg-Essen, 47048 Duisburg, Germany.

Nils Pohl is with the Institute of Integrated Systems, Ruhr University Bochum, 44801 Bochum, Germany, and also with the Fraunhofer Institute for High Frequency Physics and Radar Techniques (FHR), 53343 Wachtberg, Germany.

Digital Object Identifier 10.1109/TRS.2024.3453708

(Rx) signals to the printed circuit board (PCB)-based antennas [24], [25], [26], [27], [28], higher mm-wave and, in particular, THz systems adopt a different approach. In these systems, the antennas are seamlessly integrated into the monolithic microwave integrated circuit (MMIC), eliminating the need for any mm-wave off-chip transition [29], [30], [31], [32]. Although most MMIC metal stacks are not inherently optimized for antenna integration due to their limited height, the smaller wavelengths at higher frequencies significantly enhance the radiation efficiency when utilizing on-chip antennas [33], [34].

Another aspect that improves with higher frequencies is the radar cross section $\sigma$, which increases proportionally to $\propto f^2$ for trihedral corner reflectors and proportionally to $\propto f$ for flat plates [35, p. 14.10]. However, the physical size, i.e., the aperture of the antenna, decreases proportionally to $\lambda^2$ $(1/f^2)$ since most antennas are scaled by wavelength. Consequently, these effects compensate for each other. Moreover, the output power decreases, and the Rx noise figure (NF) increases [36, p. 375], [37], thereby deteriorating the system's dynamic range. Modern semiconductor technology can increase the circuit's and system's performance, but the level of improvement remains limited. Therefore, other approaches are needed. According to the free-space path loss equation, the overall dynamic range can be improved by increasing the antenna's aperture or, in terms of multichannel radar systems, increasing the array size since more channels improve the SNR and, as a positive side effect, the angular resolution [38].

Therefore, this article introduces a 240-GHz frequency-modulated continuous-wave (FMCW) MIMO radar chipset designed for scalable array sizes using the B11HFC SiGe BiCMOS technology [39], featuring $f_T/f_{\max} = 250/370$ GHz. The chipset comprises a 120-GHz voltage-controlled oscillator (VCO) MMIC, generating the local oscillator (LO) signal, and a transceiver (TRX) MMIC, transmitting and receiving the 240-GHz signal after doubling the LO frequency. Each TRX MMIC contains one Tx and one Rx channel and an LO feed-through structure for cascading the MMICs using ribbon bonds. The Tx chain includes amplifiers, a multiplier, and a vector modulator (VM) for adjusting the transmitting phase. The Rx chain also includes amplifiers and a multiplier, as well as a fundamental downconversion mixer using a mixer-first topology.

This article is structured as follows. Section II presents the circuit design and the manufactured MMICs. Subsequently, Section III discusses the simulation results, while Section IV provides insights into the MMIC measurement results, including the antenna analysis in Section V. Furthermore, Section VI showcases the FMCW measurements using an $8 \times 8$ MIMO array, followed by a comparative analysis with other MIMO systems in Section VII. Finally, Section VIII summarizes the findings and concludes this article.

## II. MMIC Architecture

This article introduces two MMICs for mm-wave radar applications: first, the VCO MMIC, designed for generating the LO signal at 120 GHz, and second, the TRX MMIC, designed for both transmitting and receiving at 240 GHz. In our unique approach, the 120-GHz LO signal is efficiently transferred from the VCO MMIC to one or multiple TRX MMICs using ribbon bonds, allowing for coherently coupled MMICs. Using this approach, a radar system with one Tx and one Rx antenna consists of two MMICs—the VCO MMIC and the TRX MMIC. Notably, the system's modularity is highlighted, allowing for the integration of additional MMICs by cascading multiple TRX MMICs, providing flexibility and scalability in mm-wave system design.

### A. Voltage-Controlled Oscillator MMIC

Fig. 1 depicts the VCO MMIC and its block diagram. The MMIC includes the fundamental 120-GHz VCO, which adopts the circuit topology detailed in [40]. In addition, a 31-GHz Colpitts VCO with a double varactor design is integrated into the MMIC [41], [42], [43]. The LO signal's frequency is divided by four (120 GHz/4 = 30 GHz) and is mixed with the 31-GHz signal of the auxiliary VCO. The resulting signal is stabilized using an off-chip phase-locked loop (PLL) device [29]. This offset PLL approach reduces the steep varactor characteristic, resulting in smaller division factors within the PLL and a more constant loop gain, as detailed in [42] and [44]. Simultaneously, the 31-GHz VCO is stabilized by a by-8 divider, with the 34 GHz/8 = 4.25 GHz signal fed to off-chip PLL components, generating the tuning signal through a loop filter.

The MMIC includes two passive 120-GHz branchline couplers (BLCs) and RF pads in addition to active components. The BLCs generate $IQ$ signals from the differential VCO output, connecting it to the RF pads. In the initial scalable MIMO radar version, $IQ$ signals were routed between MMICs. However, the current TRX MMIC version uses non-$IQ$ signals. Therefore, the BLC is precisely sliced with a laser cutter, omitting $IQ$ signal generation and making half of the RF pads per MMIC edge nonfunctional. The 120-GHz LO signal connections comprise small aluminum pads to minimize parasitic capacitance and a GSGSG configuration (G: ground and S: signal). In addition, we use short-circuited transmission lines (TLs), connecting the S-pad to the G-pad, to compensate for the parasitic capacitance of the S-pad. The characteristics of the pads and the used ribbon bond connection are detailed in Section IV.

### B. TRX MMIC

In the scalable system approach, the 120-GHz LO signal is connected via ribbon bonds to the TRX MMIC, which is shown in Fig. 2. Afterward, the LO signal is divided by multiple Wilkinson (WK) power dividers, needed for delivering the LO signal to each building block. One-half of the power is dedicated to the receive circuits, while one-quarter is directed to the transmit circuits. Finally, the remaining quarter is routed to the 120-GHz output pads, distributing the LO signal to the next MMIC via ribbon bonds. This power distribution and MMIC interconnectivity strategy is a key element, ensuring sufficient LO power for each transceiver part of the current MMIC, namely, the Tx and Rx channel, and for the following TRX MMIC as described in Section VI. All the circuit elements mentioned here are integrated into the $1968 \times 1448$ $\mu$m MMIC.

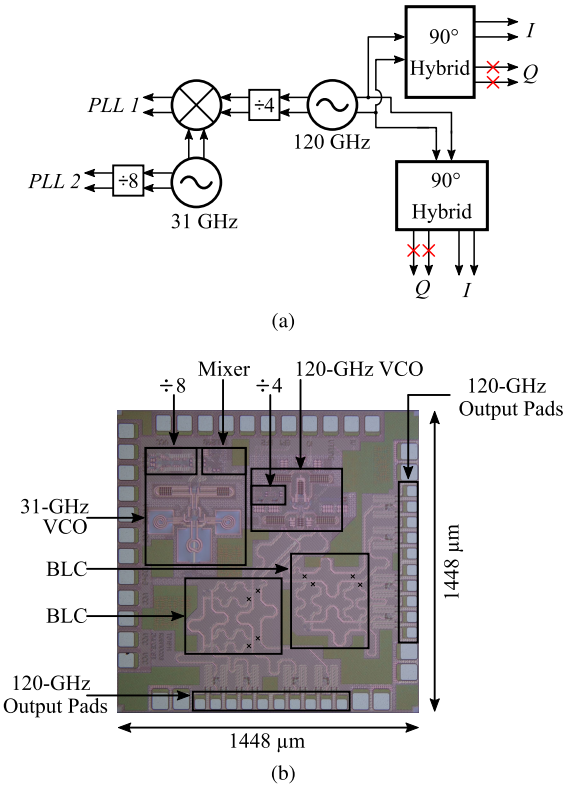


Fig. 1. (a) Block diagram and (b) photograph of the VCO MMIC, which contains the 120-GHz VCO as well as a 31-GHz VCO, a mixer, and two frequency dividers for implementing an offset PLL using off-chip surface-mounted device (SMD) components from Analog Devices (ADF 4159 [45]). Red crosses in the block diagram and black crosses in the photograph indicate the modified TLs.

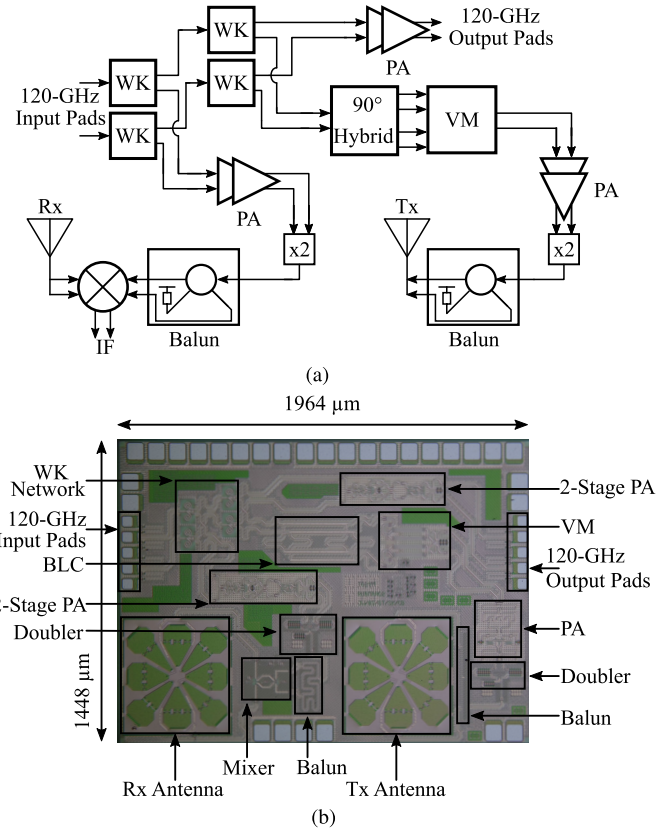


Fig. 2. (a) Block diagram and (b) photograph of the transceiver MMIC with highlighted components. The LO signal is connected via the RF input pads on the left and is transferred to the next TRX MMIC using the RF pads on the right side.

Within the Tx circuits, a sequence of components is utilized to modulate, amplify, and double the 120-GHz LO signal. This chain includes a BLC, a VM, a two-stage power amplifier (PA), a frequency doubler, a balun, and a circularly polarized differential transmit antenna [46], which uses two different resonance frequencies similar to [34]. The BLC and VM collaboratively generate eight phase states, facilitating coarse beam steering and phase inversion for applications such as phase-modulated continuous-wave (PMCW) radar and low-level digital modulation schemes for communication applications. Further details on the VM can be found in [47] and improvements are presented in [48] and [49]. The two-stage PA is designed to compensate for losses incurred by ribbon bonds and WK dividers. Moreover, the frequency doubler, utilizing a push–push topology, benefits significantly from a large input power [50, p. 1289]. The last components in the Tx chain are a TL-based balun employing the rat-race topology and an on-chip transmit antenna. The balun generates a pseudo-differential signal from the single-ended output of the doubler, connected to the differential transmit antenna.

Within the Rx chain, the LO signal is amplified by a PA, which was presented in [51]. Afterward, the LO signal's frequency is doubled using a push–push frequency multiplier [29]. The single-ended output signal is routed to a balun, which generates a pseudo-differential signal for the double-balanced mixer. The whole Tx and Rx chains are simulated, and the results are shown in Section III.

On the TRX MMIC, we use on-chip antennas that are circularly polarized. There are two main reasons for this. The VCO MMIC has RF pads on two edges to bond an LO signal to a TRX MMIC. This allows the creation of a 2-D array, enabling 3-D localization. When using circular polarization, the TRX MMICs can be rotated by 90° without decoupling the vertical MMICs from the horizontal MMICs. This is important in order to generate the largest possible number of virtual antennas in the MIMO system. Second, the Tx and Rx antennas are mirrored to each other. When the transmitted signal is reflected off a planar object or a trihedral corner reflector, the circular polarization flips. Therefore, the antennas are arranged so that they transmit a right-handed circular polarization and receive a left-handed circular polarization. This mirroring of Tx and Rx antennas has another advantage. Direct crosstalk on the TRX MMIC between the two antennas is slightly reduced. Strong low-frequency signal components in the intermediate frequency (IF) spectrum are therefore suppressed. The details of the used antenna can be found in Section V.

## III. Simulation Results

The two MMICs are based on various components needed for FMCW radar operation. While the VCOs and ribbon bond connection can be directly measured using the MMIC itself or a dedicated test structure, the transceiver circuits and couplers are characterized based on simulations. To estimate their performance, we employ either electromagnetic (EM)

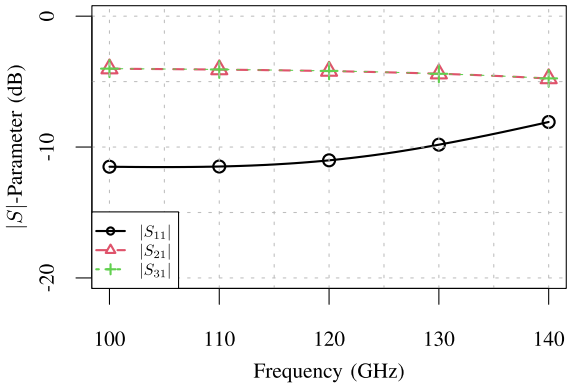


Fig. 3. EM simulation of the $S$-parameters of the lumped-element WK power divider.

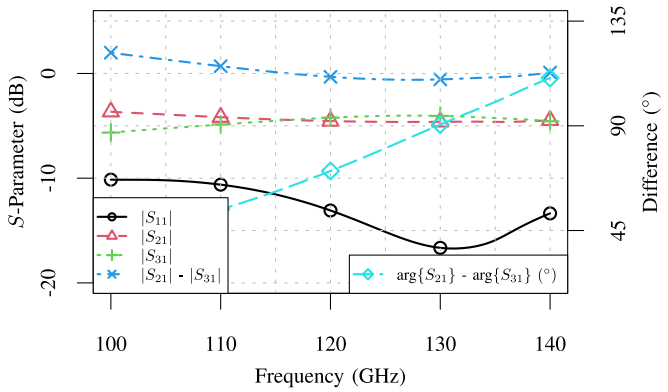


Fig. 4. EM simulation of the $S$-parameters of the TRX MMIC's BLC (90° hybrid).

simulation and/or circuit simulation incorporating resistive and capacitive parasitic elements ($RC$ parasitics).

### A. Coupler Simulation

In this section, we analyze two passive couplers that are part of the TRX MMIC: first, the WK power divider, and second, the BLC, which generates $IQ$ signals for the VM. Both couplers are simulated using Sonnet EM 18.52.

In a multi-MMIC system concept, the integration of power dividers is essential since the LO signal is used for multiple chips. Nevertheless, implementing TL-based WK power dividers causes a significant challenge due to their substantial space requirements. Furthermore, the LO feed-through concept needs additional PA stages to counteract splitting losses, consequently expanding circuit space requirements. Therefore, our presented concept adopts a lumped-element approach [52, p. 232]. Instead of utilizing $\lambda/4$ TLs for a WK divider, which would extend approximately to 300 $\mu$m in the B11FHC technology, we utilize inductors and capacitors. Four single-ended power dividers are employed to split the differential LO signal into three distinct paths. After the initial division, one half is directed to the Rx circuits, while the other undergoes a secondary split, feeding into the Tx circuits and pads for the subsequent MMIC. These four WK dividers collectively occupy an area of 290 $\times$ 335 $\mu$m, which is a significant space saving compared to TL-based WK dividers. On the TRX MMIC, we use the top copper layer in the B11HFC metal stack to create a spiral inductor with two windings. Metal–insulator–metal (MIM) capacitors are used as capacitive elements. In Fig. 3, the EM simulation results of the WK divider are depicted, showing $S_{21}$ and $S_{31}$ of $-4.2$ dB and a wideband $S_{11}$ of less than $-10$ dB below 130 GHz.

In addition to the power divider, a BLC is used to generate in-phase ($I$) and quadrature-phase ($Q$) signals for the VM, which was presented in [47]. The VM superimposes these signals, allowing for the selection of either the $I$ or $Q$ path, both paths combined, or their inverted versions, resulting in a total of eight unique phase positions (constellation points). The positions of these points (amplitude and phase) are essential for the beam steering and binary phase modulation properties. The position and spacing of these constellation points rely primarily on the $IQ$ input signals of the VM, as investigated in [47]. Fig. 4 shows a small $IQ$ amplitude imbalance (below 2 dB at lower frequencies and below 0.5 dB above 115 GHz) and a phase difference of 70° at 120 GHz and 90° at 130 GHz.

### B. Tx Chain

Fig. 5 depicts the active components within the Tx chain, which is based on three components: a two-stage 120-GHz PA followed by a frequency doubler transforming the signal from 120 to 240 GHz. The amplifier design incorporates common emitter and common base stages (cascode), which are matched through an interstage TL. The circuit uses short TLs ($<\lambda/4$) as inductive load. The interconnection between the two amplifier stages is achieved through a matching network, as depicted in the bottom center of Fig. 5. The matching network between the second PA and the frequency doubler is shown at the bottom right.

The frequency doubler is based on a push–push architecture and is illustrated in the right of Fig. 5. Its output network, featuring a TL and capacitance, transforms the output impedance to 50 Ω, followed by a rat-race-based balun essential for connecting to the differential on-chip antenna. Notably, all three stages can be activated and deactivated by switching the bias potentials to either 0 V or the correct bias voltage using an external enable signal (EN). This function is essential for the MIMO system, enabling the time-division multiplexing (TDM) functionality.

The Tx chain simulation accounts for TLs, incorporated using precise SPICE models, and $RC$ parasitics for the HBTs generated through parameter extraction using Calibre Quantus QRC. Within the Cadence Virtuoso-based circuit simulation, two key parameters are varied during the simulation: the frequency and the input power at the first PA stage. The latter variation is essential, as the power can only be roughly estimated at this point.

In the best case scenario, we assume 0-dBm input power at the first PA, and in the worst case, we assume $-20$ dBm. The exact value depends on whether the LO comes from the VCO MMIC (maximum power $\approx$ 0 dBm, cf. Section IV) or another TRX MMIC (PA's $P_{\text{sat}} \approx 6$ dBm) [51]. After the ribbon bond connection, the LO signal is attenuated by up to 6 dB (cf. Section IV). After the WK network, the LO signal

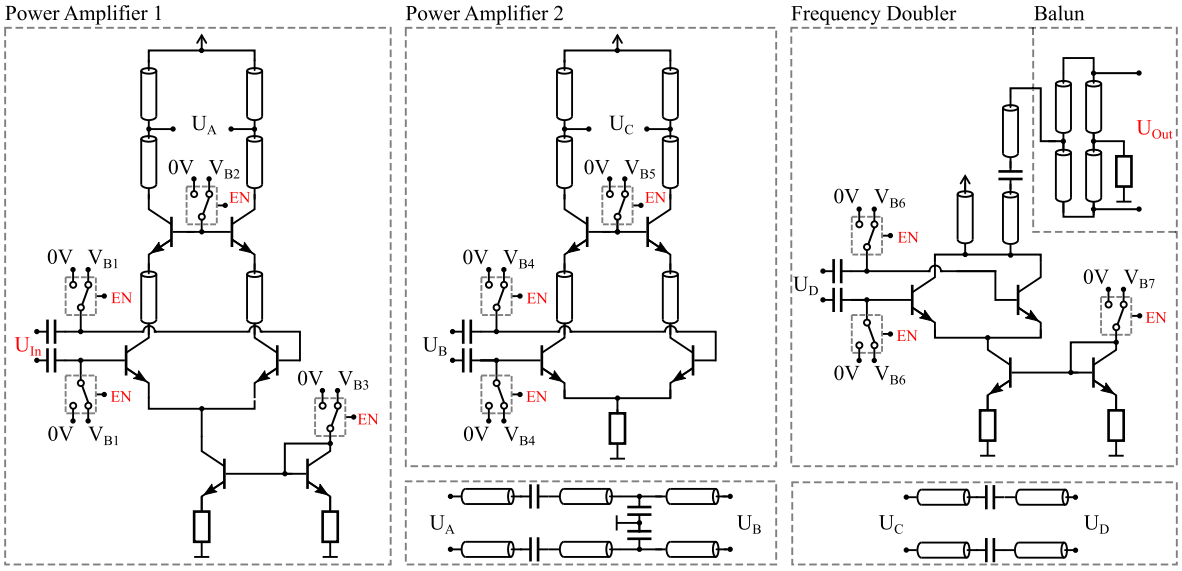


Fig. 5. Schematic of the Tx chain, which consists of two PAs and one frequency doubler stage. The PAs use a common emitter and common base stage (cascode) connected via a TL for interstage matching, and the doubler uses a push–push architecture and a rat-race balun to create a pseudo-differential output signal.

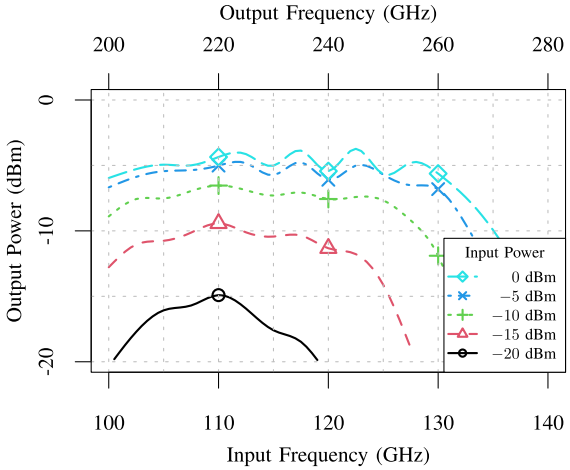


Fig. 6. Simulation results of the Tx chain using Cadence Virtuoso, including $RC$ parasitics and 80° device temperature. The used input power varies between −20 and 0 dBm since the exact number can only be roughly estimated. Above −10 dBm, the circuit shows compression effects, which limit the output power to ≈−5 dBm.

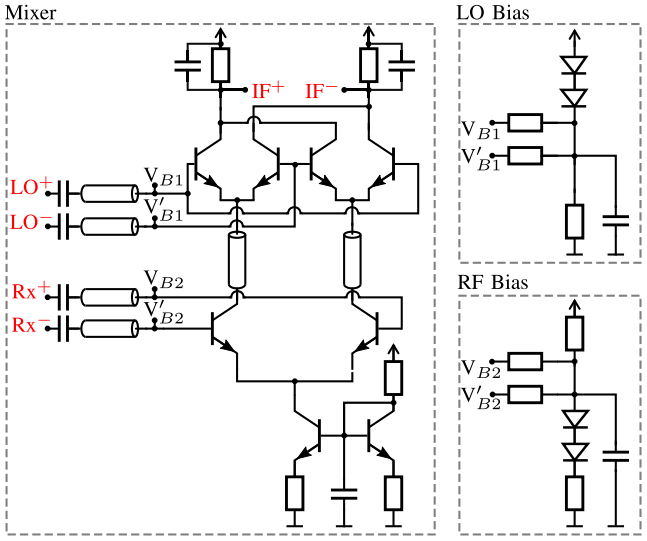


Fig. 7. Schematic of fundamental Gilbert cell mixer, consisting of a current mirror, a differential pair, and a switching quad (similar to [49]).

is attenuated by up to 8 dB. Based on the selected state of the VM, the LO signal is amplified by 0–6 dB [47]. Therefore, the LO power on the first TRX MMIC (directly after the VCO MMIC) is −14 to −8 dBm. For each following TRX MMIC, the input power at the first PA stage of the Tx chain is approximately 6 dB higher, namely, −8 to −2 dBm, since the PA of the previous TRX MMIC connected to the 120-GHz output pads has $P_{sat}$ of ≈6 dBm. Moreover, each component in the LO signal distribution is frequency-dependent with a low-pass (WK network and bond connection) or bandpass behavior (PA). Therefore, the simulation setup covers a slightly larger input power range starting from −20 and ending at 0 dBm to account for these variances.

The simulation results in Fig. 6 indicate a compression behavior beginning at −10 dBm, resulting in output powers of approximately −7 dBm at this level. The maximum saturated output power of the used PAs mainly causes the compression of the Tx chain's output power. However, at very high input powers ranging from −5 to 0 dBm, the Tx chain generates an output power of around −5 dBm.

### C. Rx Chain

Fig. 7 shows the fundamental downconversion mixer, which is based on a Gilbert cell. The mixer circuit has a current mirror that generates a dc current for the LO and Rx transistors, ensuring an optimal current density. To achieve transistor matching, a series circuit containing an MIM capacitance and a TL is used for both LO and RF transistors. The required bias voltage, depicted in Fig. 7 (right), is created using resistors and diodes, strategically chosen to minimize temperature dependence. Using a differential pair and a switching quad, the

mixing process of LO and Rx signals generates an IF signal at the resistive–capacitive load. Furthermore, the additional capacitor effectively suppresses the sum frequency ($f_{\mathrm{LO}}+f_{\mathrm{RF}}$) in the IF signal.

Behind the first WK divider (cf. Fig. 2), the Rx chain starts with a two-stage PA, which has already been published in [51] and has a gain of up to 30 dB. This gain is slightly higher than in the Tx chain because a 5-V power supply is used since no 3.3-V compatible switches must be incorporated into the circuits as the Rx chain is always on. The PA stage is followed by a frequency doubling stage with a push–push topology and a balun, which generates a differential signal needed for the double-balanced Gilbert cell mixer. The Rx port of the mixer is connected to the on-chip antenna, and the IF port is connected directly to the pads of the MMIC.

Using precise TL models and *RC* parasitics, we simulated the complete Rx chain, including the two-stage PA, frequency doubler, balun, and mixer. This analysis focused on two key metrics: conversion gain (CG), which measures the efficiency of converting the received signal voltage to the IF voltage, and NF, indicating the added internal noise compared to the received signal. As depicted in Fig. 8, the Rx chain achieves a CG of up to 12 dB when using an LO input power of 0 dBm. Even lower power levels (−10 dBm) show competitive performance. However, the CG drops for input power levels below −10 dBm as the Rx chain leaves its compression region.

The simulated NF correlates with the CG behavior: It shows minimal improvements above −10-dBm input power due to saturation. The double sideband (DSB) NF reaches its minimum (around 14–17-dB single sideband) when the CG is at its maximum. This trend arises from the inverse relationship between NF and gain. The NF increases toward the displayed upper and lower frequency limits due to nonideal matching within the mixer and nonconstant output power over frequency from the PAs and the frequency doubler.

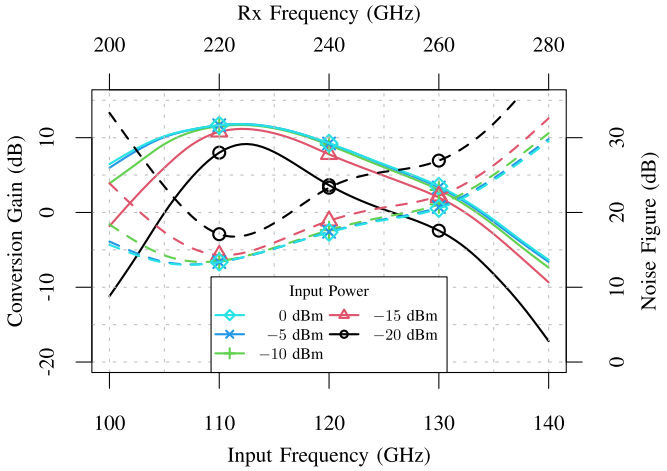


Fig. 8. Simulation results of the Rx chain using Cadence Virtuoso, *RC* parasitics, and 80 °C device temperature. The IF frequency is set to 1 MHz over the shown frequency range. The CG (solid lines) and NF (dashed lines) are shown. The input power varies between −20 and 0 dBm since the exact value can only be estimated. Compared to the Tx chain, even −20-dBm input power shows good results since a powerful PA is used.

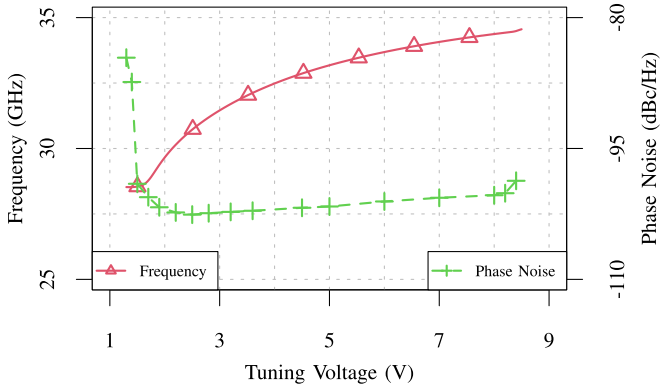


Fig. 9. Measured output frequency and phase noise of the auxiliary VCO, plotted versus the tuning voltage. The shown phase noise curve includes the adjustment of 18 dB.

## IV. MMIC Measurement Results

Section III presented the Tx and Rx chain simulation results since no breakout test structure is available. However, we can measure the dc power consumption, which is 126 mA for the 5-V supply (Rx and LO distribution) and 67 mA for the 3.3-V supply (Tx). In total, the TRX MMIC consumes 851 mW.

This section presents the measurement results of the VCO MMIC, which can be characterized directly using on-wafer probes. Moreover, we present the measurement results of the ribbon bond connection using a dedicated test structure. We characterize the VCO's tuning behavior, output power, and phase noise using a spectrum analyzer (SA) and a power meter. In addition, a vector network analyzer (VNA) equipped with frequency extender modules measures the performance of the bond wire connections.

### A. VCO MMIC

We use two VCOs on the MMIC: the first VCO generates the 120-GHz signal, which is routed to the TRX MMICs, and the second auxiliary oscillator is only for stabilization purposes, using a center frequency of 31 GHz. The analysis focuses on the phase noise, the output power, and the tuning range. The whole MMIC consumes 118 mA at 5-V power supply, which equals a power consumption of 590 mW.

The auxiliary oscillator's measurement results are depicted in Fig. 9, showing the tuning curve and the phase noise at 1 MHz offset. Both parameters were measured behind a static by-8 frequency divider. Therefore, the measured phase noise values have to be adjusted by adding 6 dB per octave, resulting in a total of 18 dB [53]. Inside the radar system, the divider is needed since commercial SMD PLL chips for frequency stabilization have a relatively limited frequency range, i.e., 13 GHz for the used ADF4159 from Analog Devices [45]. The measurements show a minimum and maximum output frequency of 28.6 and 34.5 GHz, resulting in a tuning range of 5.9 GHz and 18.7%, respectively. The lowest phase noise value is −102.5 dBc/Hz achieved at the center frequency. The VCO has a higher phase noise toward the lower and upper limits.

In contrast to the 31-GHz auxiliary VCO, the measurement setup of the 120-GHz VCO is slightly different. Direct

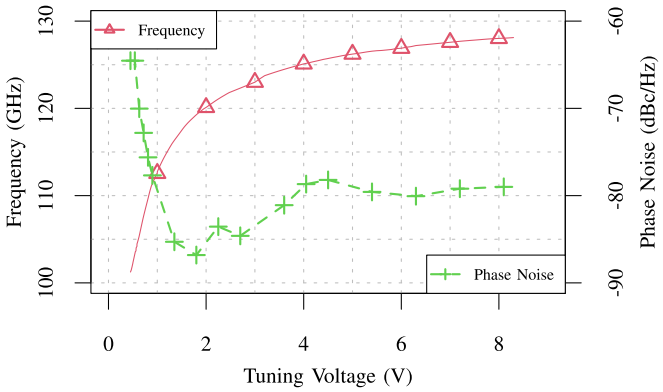


Fig. 10. Measured output frequency and phase noise of the 120-GHz VCO, plotted as function of the tuning voltage.

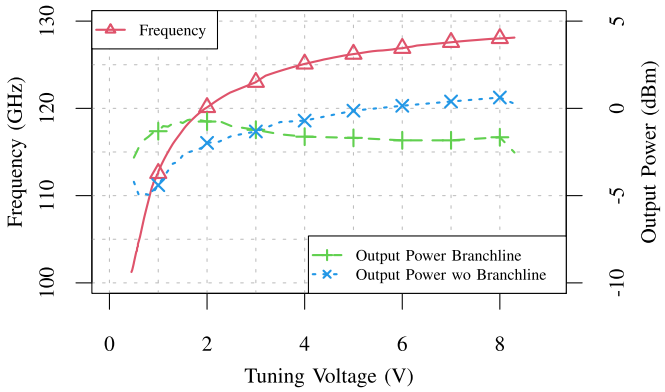


Fig. 11. Measured output frequency and output power of the 120-GHz VCO, plotted dependent on the tuning voltage. The two power curves show the characteristic depending on the state of the BLC.

measurement of the LO signal is feasible, as it is connected to standard pads on the MMIC using a pitch of 75 $\mu$m. However, one challenge arises: the R&S FSWP SA is limited to 50 GHz. To address this limitation, we employ a VDI WR-3.4 signal analyzer extension (SAX) module (N9029BV) and a Keysight PSG signal generator (E8257D) for block-down conversion, enabling the use of the FSWP within an applicable frequency range. The LO signal is mixed down into a lower frequency range, which can be measured with the SA.

Since the signal generator has a phase noise of $-145$ dBc/Hz at the 1-MHz offset, the measurement setup should not impact the VCO's phase noise measurement. In Fig. 10, the phase noise and tuning behavior measurement results are presented. Notably, the VCO exhibits a steep tuning characteristic, where the oscillation starts at approximately 0.5 V, equivalent to a frequency of 101.3 GHz. The maximum frequency reaches 128.1 GHz at 8.3 V. The minimum phase noise of approximately $-86.8$ dBc/Hz is attained at the 1-MHz offset.

At low frequencies, the phase noise is relatively high and decreases rapidly until it reaches its optimum at approximately 2 V. One reason for this is that the varactor diode's quality factor is worse at low voltages than at high ones. In addition, the design of the VCO and its phase noise performance has an optimum range. If the tuning voltage is too low, the VCO does not oscillate or shows increased phase noise since it is not yet in its steady state.

As mentioned before, the BLC is modified since the presented version of the TRX MMIC only uses a differential signal and no $IQ$ signal is provided by the VCO MMIC. The modification in the two BLCs is highlighted in Fig. 1 using small and red (block diagram) and black (MMIC photograph) cross symbols. The BLC is modified via a laser to mitigate $IQ$ signal generation and to achieve a higher output power. A higher output power is achieved because only one differential signal has to be generated per MMIC edge and no longer two ($I$ and $Q$). Consequently, a nearly 3-dB increase in power is observed.

Fig. 11 illustrates the output power, including two power curves due to the presence of a BLC within the VCO chip. The green curve represents the power curve with the BLC intact, which reduces the output power at the upper frequency range by up to 2.5 dB. However, within the radar system, the modified BLC is used, and therefore, the blue curve is only relevant, showing an output power of up to 0.6 dBm.

The power difference at higher frequencies meets the expectations when removing a coupler that splits the input power equally to both output ports. However, the power difference at lower frequencies shows a different behavior. It reverses so that the output power with BLC exceeds the output power without the coupler. This is caused by the $IQ$ imbalance of the branchline used on the VCO MMIC, which is more pronounced than on the TRX MMIC (cf. Fig. 4).

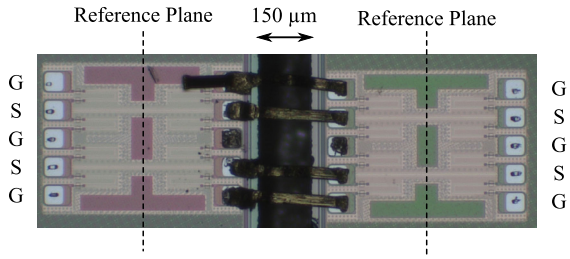


Fig. 12. Test structure to characterize the ribbon bond connection using a GSGSG pad configuration with a pad pitch of 75 $\mu$m and a gap between the MMICs of ≈150 $\mu$m. The center ribbon bond was omitted since the bonding head was not thin enough.

### B. Bond Connections

The proposed concept involves distributing the radar system's functionality onto multiple MMICs, aiming to increase the number of channels and array size. However, routing a 120-GHz signal from one MMIC to another is challenging since the MMICs' separation is in the range of one wavelength, and the impedance has to be matched to 50 Ω. Therefore, we use a 13 × 38 $\mu$m flat ribbon bonds and evaluate them on a test structure. The advantage of ribbon bonds is the suitable RF impedance since wire bonds suffer from a too-high impedance [54].

The manufactured test structure contains the same RF pads used for the VCO and TRX MMIC. The pads are placed in a back-to-back structure on the breakout MMIC. The setup includes two MMICs placed adjacent to each other with a gap of ≈150 $\mu$m between the MMIC edges, contacting

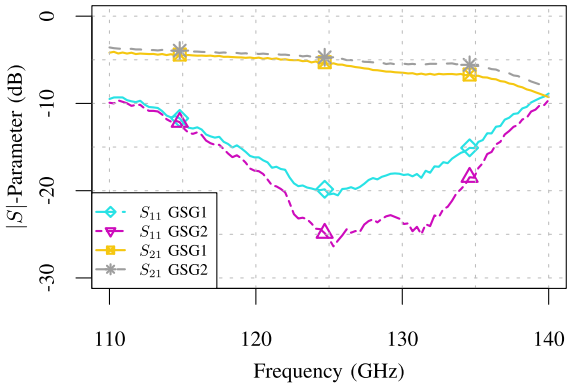


Fig. 13. Measured $S$-parameters of the back-to-back structure using $D$-band VNA extenders and GSG probes. The results are deembedded so that the reference plane is halfway between the pads (cf. Fig. 12).

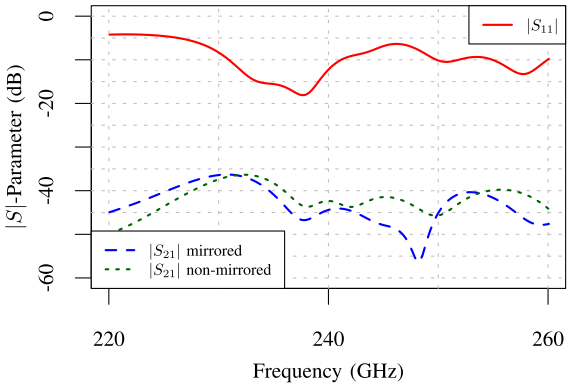


Fig. 14. Simulated crosstalk of the two antennas on the TRX MMIC. The red curve shows the input matching of the antenna, and the blue curve shows the power transferred directly from the Tx antenna to the Rx antenna. The green curve shows $S_{21}$ for the case the Rx antenna is nonmirrored, purely for investigation purposes.

the outer pads using single-ended GSG $D$-band probes, and interconnecting the inner MMIC pads using ribbon bonds. The measurement setup is detailed in Fig. 12, and the results are presented in Fig. 13. The results are deembedded so that the probed pads and half the distance of the 50-Ω TLs are removed from the results. Therefore, the results contain just two short 50-Ω microstrip TLs, two pads, and the ribbon bond connection.

Fig. 13 presents single-ended $D$-band VNA measurement results obtained with a GSG probe. Both $S_{11}$ and $S_{21}$ parameters are shown for the upper (GSG1) and lower (GSG2) contacts. Notably, the ribbon bonds achieve $S_{11}$ mostly below $-10$ dB across a broad frequency range of 30 GHz. $S_{21}$ indicates a loss of around 5 dB. The crosstalk from GSG1 on the left MMIC to GSG2 on the right MMIC is around $-25$ dB. However, this value is only meaningful when using the bonds single-ended.

The results show that 120 GHz can be used as a distribution frequency, as the losses at this frequency can be compensated for using PAs. At the same time, 120 GHz offers the advantage that only one frequency doubler is required, which improves the power consumption of the TRX MMIC. In addition, there are fewer unwanted harmonics in the Tx spectrum, which could lead to ghost targets [29], [55].

While the $S$-parameter results are not as competitive as in [56], [57], [58], and [59], the manufacturing of the ribbon bonds is as easy as every other bond connection, making it suitable for mass production.

## V. Antenna Analysis

In our concept, we utilize two antennas per TRX MMIC that interact directly. The direct coupling from one antenna to the other leads to significant signal components in the low-frequency area of the range spectrum when using FMCW chirps. As mentioned earlier, we utilize circularly polarized (CP) antennas, with the Rx antenna mirrored to the Tx antenna. This mirroring is necessary because the rotation of the CP flips when an EM wave gets reflected at a target. Theoretically, this configuration offers an advantage, as the transmitting and receiving antennas are mirrored, potentially suppressing the crosstalk. To quantify this, we simulated both antennas with a pitch of 1060 $\mu$m using Empire XPU software: once as deployed on the MMIC (mirror configuration of Tx and Rx antenna) and once in the same orientation (no mirroring). However, the aim of using the CP antennas is to rotate the MMICs to create a 2-D array. When using linearly polarized (patch) antennas, two TRX MMIC versions had to be used where one has rotated antennas.

The nonmirrored case serves only for testing purposes to quantify the suppression achieved by mirroring. The simulated $S$-parameters, including the antenna's $S_{11}$ and the crosstalk indicated by $S_{21}$ from the transmitting antenna to the receiving antenna, are depicted in Fig. 14. The direct crosstalk is rather small, measuring approximately $-40$ dB. Furthermore, in the region around 245 GHz, where the antenna exhibits excellent CP purity [46], an additional suppression of 5–10 dB is observed.

The overall coupling from the Tx into the Rx antenna shows similar behavior for both investigated cases. We conclude that the main part of the transferred energy is caused by near-field coupling between the two antennas and not by far-field coupling. Otherwise, we would expect a greater difference between the two curves.

In addition to direct crosstalk from the Tx antenna to the Rx antenna in the near field, another relevant property is the transmission behavior from the Tx to the Rx antenna in the far field. Since the MMICs can be placed on two edges of the VCO MMIC, we analyze the transmission from Tx to Rx in case they are twisted and nontwisted to each other. We use $S$-parameters measured with a linear-polarized horn antenna in $\theta$ and $\varphi$ polarization. The measurement was performed within an antenna measurement setup as described in [60]. The transmission behavior is calculated similar to [61, p. 303]. For a vertically oriented antenna (index V), the electric field in the $x$-direction arises from $S_{21}$ in the $\theta$-direction. In contrast, the electric field in the $y$-direction arises from $S_{21}$ in the $\varphi$-direction

$$E_{\mathrm{V},x} \propto S_{21,\theta}$$
$$E_{\mathrm{V},y} \propto S_{21,\varphi}. \tag{1}$$

For a horizontally oriented antenna (index H), the electric field in the $x$-direction arises from $S_{21}$ in the $\varphi$-direction with

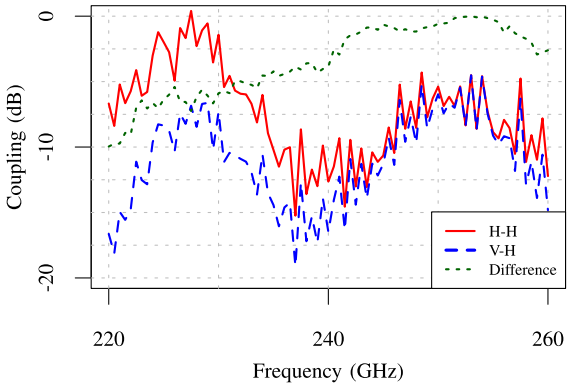


Fig. 15. Measured coupling efficiency based on (3) if the antennas are rotated the same (H–H) or rotated differently by 90° (H–V).

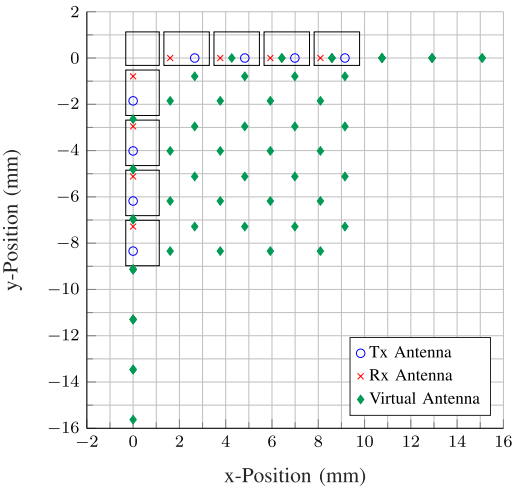


Fig. 16. MMIC placement on the front-end PCB showing the MMIC and on-chip antenna positions (red crosses and blue circles), as well as the virtual antenna's positions (green diamonds).

an inverted sign. The electric field in the $y$-direction for the horizontally oriented antenna arises from $S_{21}$ in the $\theta$-direction

$$E_{\mathrm{H},x} \propto -S_{21,\varphi}$$
$$E_{\mathrm{H},y} \propto S_{21,\theta}. \tag{2}$$

According to [61, p. 303], the coupling between differently oriented antennas can now be determined according to (3), where $\{\cdot\}^*$ indicates the conjugation of complex values. We examine the case for two equally oriented antennas (H–H) and two differently oriented antennas, where one is horizontally oriented and one is vertically oriented (V–H). We also investigate the difference between the two couplings, as depicted in Fig. 15. Good circular polarization is achieved at frequencies around 250 GHz. The difference between both cases is minimal. However, circular polarization is not ideal for low frequencies, resulting in additional attenuation when the Tx and Rx antennas are not similarly oriented. The nonideal CP can also be recognized by the difference between the red (H–H) and blue (V–H) measurement curve, which is shown as a green dotted curve

$$C_{\mathrm{H–H}} \propto E_{\mathrm{H},x} \cdot E^*_{\mathrm{H},x} + E_{\mathrm{H},y} \cdot E^*_{\mathrm{H},y}$$
$$C_{\mathrm{V–H}} \propto E_{\mathrm{V},x} \cdot E^*_{\mathrm{H},x} + E_{\mathrm{V},y} \cdot E^*_{\mathrm{H},y}. \tag{3}$$

Besides the coupling between Tx and Rx antennas, the virtual array is a key aspect of an MIMO radar system. Fig. 16 shows the MMIC placement on the system's front-end PCB, where each MMIC is depicted as a rectangular box and each physical antenna with a blue circle (Tx—positioned at $\mathbf{r}_{\mathrm{Tx}}$) or a red cross (Rx—positioned at $\mathbf{r}_{\mathrm{Rx}}$) using the following equation:

$$\mathbf{r}_{\mathrm{Tx}} = [\vec{r}_1, \ldots, \vec{r}_{N_{\mathrm{Tx}}}]^T \in \mathbb{R}^{N_{\mathrm{Tx}} \times 3}$$
$$\mathbf{r}_{\mathrm{Rx}} = [\vec{r}_1, \ldots, \vec{r}_{N_{\mathrm{Rx}}}]^T \in \mathbb{R}^{N_{\mathrm{Rx}} \times 3}. \tag{4}$$

Since each TRX MMIC contains one Tx and one Rx antenna, the virtual array has a nonrectangular shape with virtual elements extending beyond the virtual array's core area. The virtual antenna position is calculated with a Kronecker product of the Tx and Rx position, as outlined in (5). The vector $\mathbf{1}_N$ contains only ones and has a dimension of $N \times 1$ according to the number $N$ of physical Tx and Rx antennas [38], [62, p. 20]

$$\mathbf{r}_{N_v} = \mathbf{r}_{\mathrm{Tx}} \otimes \mathbf{1}_{N_{\mathrm{Rx}}} + \mathbf{1}_{N_{\mathrm{Tx}}} \otimes \mathbf{r}_{\mathrm{Rx}}. \tag{5}$$

The closest spacing in the $x$- and $y$-directions between the virtual elements positioned at $\mathbf{r}_{N_v}$ is ≈1.1 mm, which is slightly shorter than the used wavelength at 240 GHz (≈1.25 mm).

## VI. System Measurements

The results shown so far have been limited to individual components or subsystems. In this section, system measurements are presented, and both the radiated power and the FMCW spectra are analyzed. For this purpose, we have constructed an MIMO system with eight MMICs, resulting in $8 \times 8 = 64$ virtual channels. Four MMICs were placed horizontally and four MMICs were placed vertically next to the VCO MMIC, creating a colocated MIMO array [63]. The LO signal is generated by the VCO MMIC and fed to all TRX MMICs to ensure coherent operation. The layout of the MMICs on the front-end PCB is shown in Fig. 17 (side). Although we operate at a center frequency of 240 GHz, only FR4 is used as PCB substrate material. This is possible because no signals above 8 GHz (PLL input) are routed over the FR4 PCB. Furthermore, the 120-GHz LO signal is routed from MMIC to MMIC, and the antenna is also located on the MMIC itself. This is a significant advantage of the concept presented here. The PCB technology can be simplified despite the considerably higher center frequency than conventional 77-GHz automotive systems. However, placing the MMICs and bonding them to PCB and each other is more complex. The MMICs were placed by hand under a microscope, and the ribbon bonds were created using a manual bonder from TPT.

The right of Fig. 17 illustrates the backside of the front end, but this time with a complete view. The L-shaped structure in the center of the PCB shows the position of the MMICs. Right next to the MMICs on the front end's backside, we use capacitors to ensure a stable power supply.

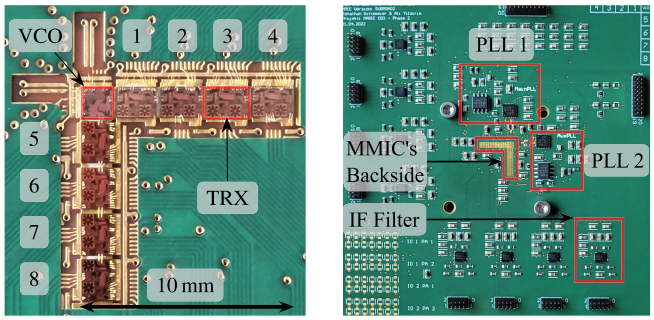


(a) (b)

Fig. 17. (a) FR4-based front-end PCB of the radar system, including the nine MMICs glued to the PCB and bonded to each other and to the PCB. (b) Backside of the front-end PCB includes two PLL circuits and eight IF amplifier channels.

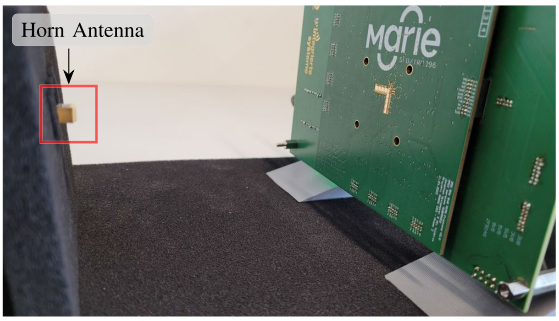


Fig. 18. Measurement setup using a Keysight signal analyzer (UXA) and a $J$-band SA extender, equipped with a horn antenna, which is surrounded by absorbers. The MIMO radar system is on the right side at a distance of 12 cm, which ensures the far-field operation.

PLL circuits needed to stabilize the two VCOs and to create the FMCW chirps are also placed close to the MMICs. There are also eight IF amplifiers on the backside, consisting of two operational amplifiers each, which are integrated into one QFN package. A total of ten pin headers connect the front end with a field-programmable gate array (FPGA), analog-to-digital converters (ADCs), and the power supply, which are located on the back-end PCB.

### A. Radiated Power

The SiGe circuits in the system are designed so that each transmit channel operates at the same power level. After splitting the LO signal on the TRX MMIC, where the power is divided for the Tx, Rx, and next MMIC, a two-stage PA is employed on the TRX MMIC. This is intended to compensate for the losses incurred during the power division and the ribbon bond connection. To validate the system concept and circuit design, the radiated power of each Tx channel is measured. For this purpose, an SAX (N9029AV03) and a Keysight signal analyzer (UXA N9041B) are utilized. Using a 20-dB horn antenna from Millimeter Wave Products Inc. (261J-20/387) and the SAX, the received power is captured and converted into the equivalent isotropically radiated power (EIRP) of the channel using the Friis transmission equation [64, p. 89], including an antenna gain $\approx -3$ dB [46]. Fig. 18 illustrates the measurement setup, and Fig. 19 shows the recorded power data for broadside radiation.

In both plots, the curves reach approximately the same maxima of about 0–1.5 dBm. In addition, the measurement curves exhibit relatively slight variation, which could be attributed to the amplifiers on the MMIC being adequately dimensioned and in saturation, ensuring sufficient power is available for each MMIC. Furthermore, it is noticeable that the power increases from one Tx MMIC to the next, which can be attributed to the PAs working in saturation. However, there is still a difference between the horizontal and vertical groups: In the horizontal case, the output power of the first two MMICs in the row (Tx1 and Tx2) is lower for low frequencies. This suggests that the ribbon bond connection is not identical for every MMIC due to manufacturing tolerances.

SA-based free-space power measurements rely on many assumptions that influence the result. The accuracy of the specified horn antenna gain, SAX CG, cable losses, and the SA detector play a crucial role in determining the output power. Since the free-space path loss is too high, we cannot cross-check the results with a power meter. Although the measured EIRP is slightly higher than the simulated output power of the Tx chain, it is in good agreement with a previous publication using a similar circuit topology, which is also based on the B11HFC technology and also reaches $\approx$0 dBm [40]. In the circuit simulation, we assumed 80 °C MMIC temperature to consider self-heating. When reducing the temperature to 40 °C, the power increases by up to 2 dB, which fits better with the measurement results. As the on-chip temperature can only be estimated, an on-chip temperature sensor is planned for the next MMIC version to get the correct temperature and to perform the circuit simulation with the precise temperature values.

### B. FMCW Measurements

Fig. 20 illustrates the IF spectra with normalized power (NP) of the 8th receive channel and all eight transmit channels. A corner reflector with an edge length of 35 mm was utilized, and 4 ms chirps with 30-GHz bandwidth are generated. While the subfigures depict the behavior of the 8th Rx antenna, the performance for other Rx channels is very similar. These subplots can be divided into two groups: the first group includes Tx1–Tx4, as these four channels are rotated 90° relatively to Rx8, while the second group comprises Tx5–Tx8, where the four channels are oriented equally to Rx8. Two distinct features are immediately noticeable: the rotated channels (Tx1–Tx4) have less dynamic range and a wider peak. As shown, this is attributed to the circularly polarized antennas, whose polarization properties are frequency-dependent, leading to less received power in the lower frequency range when rotating the Tx and Rx antennas relative to each other. Consequently, the nonrotated configuration (Tx5–Tx8) demonstrates better performance. Furthermore, another behavior is observed: the width and position of the peaks vary depending on the MMIC's position in the MIMO array. First, the position shifts due to the LO signal experiencing additional propagation delay caused by the LO feed-through structure. Second, the group delay influences the peak's width when the LO signal is transferred through multiple PA stages. As outlined in [65],

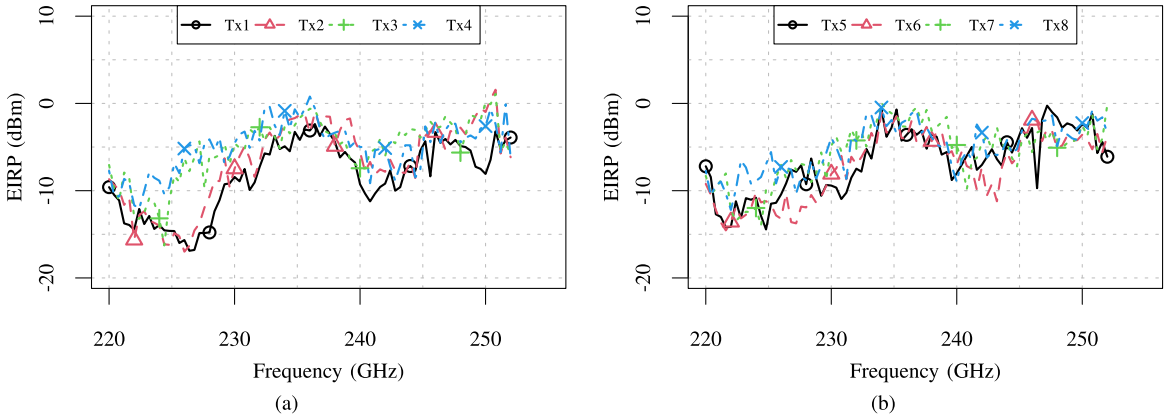


Fig. 19. Measured output power of the MIMO radar system using the measurement setup depicted in Fig. 18. (a) Horizontally orientated MMICs. (b) Vertically orientated MMICs. The power measurement was performed once for each perpendicular polarization and summed up since the used horn antenna only captures linear-polarized fields.

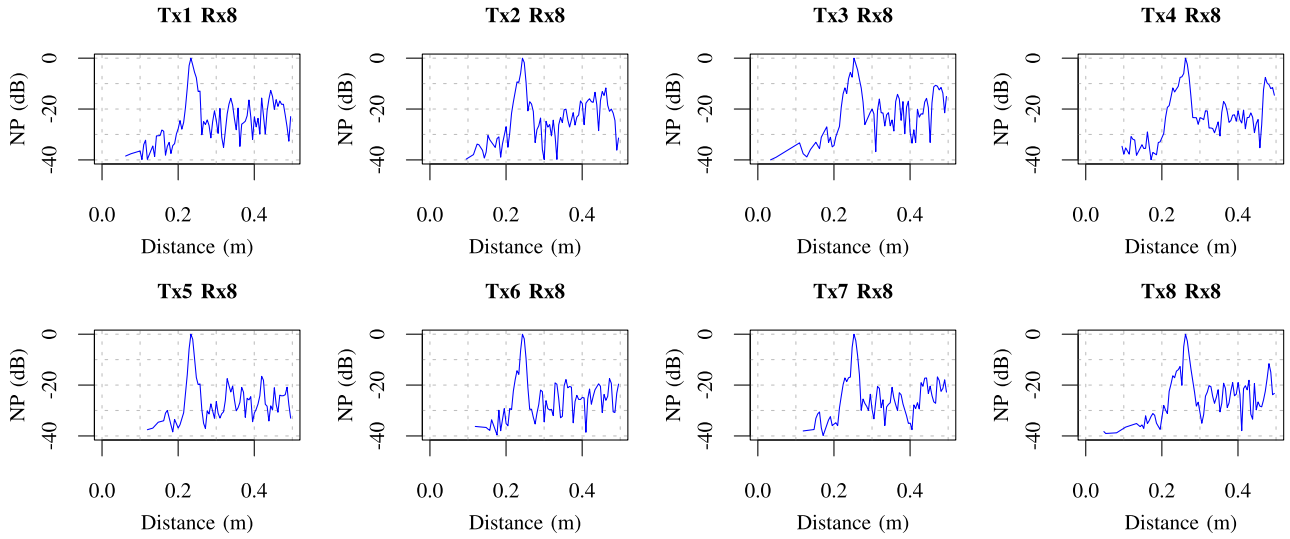


Fig. 20. Measured and NP of the IF spectra of the radar system using a front end with 8 × 8 transceiver MMICs. The transmitted signals utilize TDM. Therefore, we plotted the virtual received signals for the 8th receive antenna and all transmit antennas.

group delay broadens the peak in an FMCW system. Overall, at a frequency of 240 GHz and a distance of ≈25 cm, an SNR of 20 dB can be achieved using a rather tiny 35-mm reflector. However, when employing MIMO algorithms such as fast Fourier transform (FFT)-based imaging, an additional gain in SNR is obtained as multiple channels are evaluated simultaneously [66]. More detailed investigations into MIMO imaging with the system will be presented in later articles.

The LO feedthrough structure and the cascadable TRX MMICs cause a significant delay, which shifts the IF peak toward larger distances. In Fig. 20, the peak's position depends on the used Tx and Rx channels. The time delay can be compensated by multiplying $e^{-j\omega\tau}$ to the IF signal, where $\tau$ has to be measured for all virtual channels using a reference measurement. Moreover, the variation of radiated power of each virtual channel must be considered when performing imaging algorithms.

## VII. Comparison

First silicon-based 240-GHz ISM band signal generators and transceiver circuits appeared over a decade ago [40], [67], [68] and improved design approaches were published in the meantime [29], [69], [70], [71], [72], [73], [74], [75], [76], [77]. However, these approaches focus on single-channel designs, allowing for distance measurements only or SAR imaging when using mechanical positioning systems. Besides the upper mm-wave region, fully integrated single-channel THz sources, Rxs, and transceivers have been shown recently [15], [78], [79], [80], [81], [82].

When aiming for 3-D imaging without moving the sensor, multichannel MMICs and systems are needed. In the 77-GHz automotive band, first MIMO systems appeared roughly 15 years ago [26] and more advanced implementation followed [83], [84], [85]. Also, in the *D*-band, many results were published [24], [25], [27], [86], [87], [88], [89], [90], [91], [92], [93], [94], [95], [96]. However, above 170 GHz, the number of publications shrinks tremendously.

In the 240-GHz ISM band, Mangiavillano et al. [30] implement four Tx and four Rx antennas into a 16.2 mm$^2$ MMIC using compact on-chip antennas. The antennas create a virtual array with 0.625 mm $= 0.5\lambda$ spacing, which is slightly shorter than the 1.1 mm $= 0.88\lambda$ achieved in this article. However,

TABLE I
STATE-OF-THE-ART SILICON-BASED MIMO RADAR TRANSCEIVERS OR SYSTEMS ABOVE *D*-BAND

| Ref. | Frequency$^{\diamond}$ (GHz) | MMIC Process | $f_T/f_{max}$ (GHz) | Multiplex Mode | MMIC Area (mm$^2$) | Tx × Rx Channels | System Demonstrator | Peak EIRP (dBm) | Min. SSB NF (dB) |
|---|---|---|---|---|---|---|---|---|---|
| [32] | 223 – 276 | 130 nm SiGe (SG13G2) | 300/500 | TDM | 2.7$^{\spadesuit}$ | 1 TRX | 1 TRX | 27$^{\ddagger}$ | 18.7 |
| [31] | 234 – 254 | 130 nm SiGe (SG13G2) | 300/500 | TDM | 3.3$^{\spadesuit}$ | 1 × 1 | 1 × 1 | −5.4 | 23.5$^{\sharp}$ |
| [30] | 233 – 257 | 130 nm SiGe (B11HFC) | 250/370 | TDM | 16.2$^{\spadesuit}$ | 4 × 4 | 4 × 4 | ≈ −5 | 14.9 |
| This | 220 – 253 | 130 nm SiGe (B11HFC) | 250/370 | TDM/CDM | LO: 2.1 TRX: 2.8 | 1 × 1 | 8 × 8 | 1.5 | 17$^{\sharp}$ |

*Note:* $^{\diamond}$: Demonstrator system, $^{\ddagger}$: Using a 26 dBi lens, $^{\spadesuit}$: Without LO generation, $^{\sharp}$: Simulated

Hasan et al. [31] and Turkmen et al. [32] use a different approach. Instead of designing a large MMIC, the functionality is kept minimal on the MMIC because only one Tx and one Rx channel are implemented. Therefore, the MIMO capability is achieved by using multiple MMICs inside a radar system. This methodology is similar to this article but with different front-end circuits. These three publications and the present MMIC and system are included in Table I. All four MMICs achieve similar performance values for Rx NF and EIRP, as all use similar semiconductor technologies, namely, IHP SG13G3 or Infineon B11HFC. However, our approach is the only one that implements a VM. Also, we use a rather high LO distribution frequency of 120 GHz, while others use 12–32 GHz and route the LO signal over the front-end PCB, which makes RF substrates necessary.

In addition to the circuit's performance metrics, it is important to compare how easily the system can be scaled up and how multiple MMICs can be cascaded together. All three studies under comparison allow for the use of multiple MMICs. In [32], a frequency range of 12–15 GHz needs to be connected to the TRX MMIC and an injection-locked VCO. As a result, the LO signal must be distributed to the MMICs in a star configuration. A similar setup is shown in [30], where each MMIC requires its own 20-GHz LO signal. In both cases, the distance at which the MMICs can be placed depends on how much space is needed for the bond wires and the traces on the PCB.

However, Hasan et al. [31] use a different approach. The 32-GHz LO signal is divided on the MMIC and routed to the opposite side of the MMIC. This is similar to the method described in this article since it enables cascading multiple MMICs in a row. However, in [31], the MMICs cannot be positioned closely together because the edge of the MMIC containing the LO signals also includes other signal pads. Therefore, the LO signal has to be bonded onto the front-end PCB and not directly to the next MMIC.

Finally, Kahl et al. [97] present a 12 × 64 array using 64 Rx MMICs, which were presented in [98] and 12 commercial waveguide-based Tx modules. This approach uses widely separated antennas [99] with many wavelengths between the channels, which is somehow compensated using directive, lens-based antennas. Since this approach is not entirely based on SiGe, it is not included in Table I.

Besides silicon technologies, also III/V-based MMICs are used to build MIMO arrays for imaging when using multiple modules [100], [101], [102]. Moreover, near-field readout systems and [103] and communication MMICs have been presented [104].

## VIII. CONCLUSION

In summary, this article introduced a 240-GHz FMCW MIMO radar chipset designed for scalable array sizes using Infineon's B11HFC SiGe bipolar complementary metal-oxide-semiconductor (BiCMOS) technology, featuring $f_T/f_{max} = 250/370$ GHz. The chipset comprises a 120-GHz VCO MMIC for generating the LO signal and a transceiver MMIC for transmitting and receiving at 240 GHz. Each TRX MMIC contains one Tx and one Rx channel, which is capable of cascading multiple MMICs. The system concept involves the efficient transfer of the LO signal using low-loss ribbon bonds, enabling coherently coupled MMICs and a scalable radar system design.

Furthermore, system measurements were conducted using an MIMO system with eight MMICs, grouped into four horizontally and four vertically aligned TRX MMICs resulting in 64 virtual channels. In the MIMO demonstrator system, the front-end PCB is made of FR4 even though the operating frequency is the *J*-band, which is enabled by using frequency divider circuits on the VCO MMIC and on-chip antennas on the TRX MMICs. The coupling between the rotated and nonrotated MMICs was analyzed since circular polarized antennas are used. The analysis shows a pure circular polarization at 240 GHz, which declines toward 220 GHz. Moreover, we measured up to 1.5-dBm EIRP and performed FMCW radar measurements using commercial PLL SMD components, creating 30-GHz chirps and showing a dynamic range ≈ 20 dB.

Overall, the demonstrated radar chipset presents a significant advancement in mm-wave radar technology, offering high integration density, modularity, and scalability. In upcoming

research, we will investigate the needed calibration schemes of the system to use the VMs and to perform coherent radar imaging using the colocated 8 × 8 array.

## ACKNOWLEDGMENT

The authors thank Infineon Technologies AG for manufacturing and providing the MMICs, and Klaus Aufinger for his consultation. They would also like to thank Lukas Dierkes, the technician at the Institute of Integrated Systems, for creating the bond connections and the 3-D printed radar fixture.

## REFERENCES

[1] S. Sun, A. P. Petropulu, and H. V. Poor, "MIMO radar for advanced driver-assistance systems and autonomous driving: Advantages and challenges," *IEEE Signal Process. Mag.*, vol. 37, no. 4, pp. 98–117, Jul. 2020.

[2] C. Waldschmidt, J. Hasch, and W. Menzel, "Automotive radar—From first efforts to future systems," *IEEE J. Microw.*, vol. 1, no. 1, pp. 135–148, Jan. 2021.

[3] Y. Kalkan, "20 years of MIMO radar," *IEEE Aerosp. Electron. Syst. Mag.*, vol. 39, no. 3, pp. 28–35, Mar. 2024.

[4] D. A. Robertson, D. G. Macfarlane, and T. Bryllert, "A 220 GHz 3D imaging radar with sub-cm voxel resolution for security applications," in *Proc. 46th Eur. Microw. Conf. (EuMC)*, London, U.K., Oct. 2016, pp. 1545–1548.

[5] D. A. Robertson et al., "A high frame rate, 340 GHz 3D imaging radar for security," in *Proc. IEEE Radar Conf. (RadarConf18)*, Oklahoma City, OK, USA, Apr. 2018, pp. 0055–0060.

[6] S. S. Ahmed, A. Schiessl, and L. Schmidt, "A novel fully electronic active real-time imager based on a planar multistatic sparse array," *IEEE Trans. Microw. Theory Techn.*, vol. 59, no. 12, pp. 3567–3576, Dec. 2011.

[7] S. S. Ahmed, A. Genghammer, A. Schiessl, and L.-P. Schmidt, "Fully electronic *E*-band personnel imager of 2 $m^2$ aperture based on a multistatic architecture," *IEEE Trans. Microw. Theory Techn.*, vol. 61, no. 1, pp. 651–657, Jan. 2013.

[8] S. S. Ahmed, "Microwave imaging in security—Two decades of innovation," *IEEE J. Microw.*, vol. 1, no. 1, pp. 191–201, Jan. 2021.

[9] M. Kahl, C. Weisenstein, R. Hussung, A. Keil, F. Friederich, and P. H. Bolìvar, "MIMO design of $12 \times 64$ element polarization sensitive SiGe array for 3D in-line detection of defects at 220–260 GHz," in *Proc. 47th Int. Conf. Infr., Millim. THz Waves (IRMMW-THz)*, Delft, The Netherlands, Aug. 2022, pp. 1–2.

[10] T. Merkle et al., "Broadband 240-GHz radar for non-destructive testing of composite materials," *IEEE J. Solid-State Circuits*, vol. 54, no. 9, pp. 2388–2401, Sep. 2019.

[11] M. A. Richards, *Fundamentals of Radar Signal Processing*. New York, NY, USA: McGraw-Hill, 2014.

[12] D. Kissinger, G. Kahmen, and R. Weigel, "Millimeter-wave and terahertz transceivers in SiGe BiCMOS technologies," *IEEE Trans. Microw. Theory Techn.*, vol. 69, no. 10, pp. 4541–4560, Oct. 2021.

[13] T. Zimmer et al., "SiGe HBTs and BiCMOS technology for present and future millimeter-wave systems," *IEEE J. Microw.*, vol. 1, no. 1, pp. 288–298, Jan. 2021.

[14] P. Hillger et al., "Toward mobile integrated electronic systems at THz frequencies," *J. Infr., Millim., THz Waves*, vol. 41, no. 7, pp. 846–869, Jun. 2020.

[15] J. Wittemeier, F. Vogelsang, D. Starke, H. Rücker, and N. Pohl, "A SiGe based 0.48 THz signal source with 45 GHz tuning range," in *Proc. 51st Eur. Microw. Conf. (EuMC)*, London, U.K., Apr. 2022, pp. 869–872.

[16] T. Bryllert, M. Bonmann, and J. Stake, "A submillimeter-wave FMCW pulse-Doppler radar to characterize the dynamics of particle clouds," *IEEE Trans. THz Sci. Technol.*, vol. 13, no. 4, pp. 389–395, Jul. 2023.

[17] A. Reinhardt, L. Freiwald, T. Jaeschke, N. Pohl, and M. Höft, "A fully integrated SiGe radar sensor for aerosol flow rate measurements," *IEEE Microw. Wireless Compon. Lett.*, vol. 30, no. 2, pp. 216–218, Feb. 2020.

[18] X. Zhang, T. Chang, Z. Wang, and H.-L. Cui, "Three-dimensional terahertz continuous wave imaging radar for nondestructive testing," *IEEE Access*, vol. 8, pp. 144259–144276, 2020.

[19] K. Schmalz, A. Glück, N. Rothbart, A. Güner, M. H. Eissa, and H.-W. Hübers, "Transmitter and receiver in 0.13 $\mu$m SiGe for gas spectroscopy at 222–270/444–540 GHz," *IEEE J. Microw.*, vol. 2, no. 4, pp. 582–591, Oct. 2022.

[20] Z. D. Taylor et al., "THz medical imaging: In vivo hydration sensing," *IEEE Trans. THz Sci. Technol.*, vol. 1, no. 1, pp. 201–219, Sep. 2011.

[21] U. R. Pfeiffer et al., "Ex vivo breast tumor identification: Advances toward a silicon-based terahertz near-field imaging sensor," *IEEE Microw. Mag.*, vol. 20, no. 9, pp. 32–46, Sep. 2019.

[22] J. F. Federici et al., "THz imaging and sensing for security applications—Explosives, weapons and drugs," *Semicond. Sci. Technol.*, vol. 20, no. 7, pp. S266–S280, Jun. 2005.

[23] K. B. Cooper, R. J. Dengler, N. Llombart, B. Thomas, G. Chattopadhyay, and P. H. Siegel, "THz imaging radar for standoff personnel screening," *IEEE Trans. THz Sci. Technol.*, vol. 1, no. 1, pp. 169–182, Sep. 2011.

[24] S. Kueppers, H. Cetinkaya, R. Herschel, and N. Pohl, "A compact $24 \times 24$ channel MIMO FMCW radar system using a substrate integrated waveguide-based reference distribution backplane," *IEEE Trans. Microw. Theory Techn.*, vol. 68, no. 6, pp. 2124–2133, Jun. 2020.

[25] S. Kueppers, H. Cetinkaya, and N. Pohl, "A compact 120 GHz SiGe:C based $2 \times 8$ FMCW MIMO radar sensor for robot navigation in low visibility environments," in *Proc. Eur. Radar Conf. (EURAD)*, Nuremberg, Germany, Oct. 2017, pp. 122–125.

[26] R. Feger, C. Wagner, S. Schuster, S. Scheiblhofer, H. Jager, and A. Stelzer, "A 77-GHz FMCW MIMO radar based on an SiGe single-chip transceiver," *IEEE Trans. Microw. Theory Techn.*, vol. 57, no. 5, pp. 1020–1035, May 2009.

[27] H. J. Ng, R. Hasan, and D. Kissinger, "A scalable four-channel frequency-division multiplexing MIMO radar utilizing single-sideband delta–sigma modulation," *IEEE Trans. Microw. Theory Techn.*, vol. 67, no. 11, pp. 4578–4590, Nov. 2019.

[28] P. Kwiatkowski, A. Orth, and N. Pohl, "Combining 77–81 GHz MIMO FMCW radar with frequency-steered antennas: A case study for 3D target localization," *Int. J. Microw. Wireless Technol.*, early access, pp. 1–9, 2024, doi: 10.1017/S1759078724000254.

[29] S. Thomas, C. Bredendiek, and N. Pohl, "A SiGe-based 240-GHz FMCW radar system for high-resolution measurements," *IEEE Trans. Microw. Theory Techn.*, vol. 67, no. 11, pp. 4599–4609, Nov. 2019.

[30] C. Mangiavillano, A. Kaineder, T. Wagner, and A. Stelzer, "A 240-GHz 4-TX 4-RX 2-D-MIMO FMCW radar transceiver in 130-nm SiGe BiCMOS," *IEEE Microw. Wireless Technol. Lett.*, vol. 33, no. 8, pp. 1239–1242, Aug. 2023.

[31] R. Hasan, M. H. Eissa, W. A. Ahmad, H. J. Ng, and D. Kissinger, "Wideband and efficient 256-GHz subharmonic-based FMCW radar transceiver in 130-nm SiGe BiCMOS technology," *IEEE Trans. Microw. Theory Techn.*, vol. 71, no. 1, pp. 59–70, Jan. 2023.

[32] E. Turkmen et al., "A 223–276-GHz cascadable FMCW transceiver in 130-nm SiGe BiCMOS for scalable MIMO radar arrays," *IEEE Trans. Microw. Theory Techn.*, vol. 71, no. 12, pp. 5393–5412, Dec. 2023.

[33] H. Sobal, "Radiation conductance of open-circuit microstrip (correspondence)," *IEEE Trans. Microw. Theory Techn.*, vol. MTT-19, no. 11, pp. 885–887, Nov. 1971.

[34] B. Sievert, J. T. Svejda, J. Wittemeier, N. Pohl, D. Erni, and A. Rennings, "Equivalent circuit model separating dissipative and radiative losses for the systematic design of efficient microstrip-based on-chip antennas," *IEEE Trans. Microw. Theory Techn.*, vol. 69, no. 2, pp. 1282–1294, Feb. 2021.

[35] M. I. Skolnik, *Radar Handbook*, 3rd ed., New York, NY, USA: McGraw-Hill, 2008.

[36] S. Voinigescu, *High-Frequency Integrated Circuits* (The Cambridge RF and Microwave Engineering Series). Cambridge, U.K.: Cambridge Univ. Press, 2013.

[37] E. Johnson, "Physical limitations on frequency and power parameters of transistors," in *Proc. IRE Int. Conv. Rec.*, vol. 13, New York, NY, USA, 1965, pp. 27–34.

[38] J. Wittemeier, A. M. Ahmed, T. N. Tran, A. Sezgin, and N. Pohl, "3D localization using a scalable FMCW MIMO radar design," in *Proc. German Microw. Conf. (GeMiC)*, Cottbus, Germany, Mar. 2020, pp. 100–103.

[39] J. Böck et al., "SiGe HBT and BiCMOS process integration optimization within the DOTSEVEN project," in *Proc. IEEE Bipolar/BiCMOS Circuits Technol. Meeting*, Boston, MA, USA, Oct. 2015, pp. 121–124.

[40] C. Bredendiek, N. Pohl, T. Jaeschke, K. Aufinger, and A. Bilgic, "A 240 GHz single-chip radar transceiver in a SiGe bipolar technology with on-chip antennas and ultra-wide tuning range," in *Proc. IEEE Radio Freq. Integr. Circuits Symp. (RFIC)*, Seattle, WA, USA, Jun. 2013, pp. 309–312.

[41] N. Pohl, H.-M. Rein, T. Musch, K. Aufinger, and J. Hausner, "SiGe bipolar VCO with ultra-wide tuning range at 80 GHz center frequency," *IEEE J. Solid-State Circuits*, vol. 44, no. 10, pp. 2655–2662, Oct. 2009.

[42] N. Pohl, T. Klein, K. Aufinger, and H.-M. Rein, "A low-power wideband transmitter front-end chip for 80 GHz FMCW radar systems with integrated 23 GHz downconverter VCO," *IEEE J. Solid-State Circuits*, vol. 47, no. 9, pp. 1974–1980, Sep. 2012.

[43] S. Thomas, C. Bredendiek, and N. Pohl, "Comparison of inductor types for phase noise optimized oscillators in SiGe at 34 GHz," in *Proc. German Microw. Conf.*, Nuremberg, Germany, Mar. 2015, pp. 288–291.

[44] N. Pohl, T. Jaeschke, and K. Aufinger, "An ultra-wideband 80 GHz FMCW radar system using a SiGe bipolar transceiver chip stabilized by a fractional-N PLL synthesizer," *IEEE Trans. Microw. Theory Techn.*, vol. 60, no. 3, pp. 757–765, Jan. 2012.

[45] *Analog Devices ADF4159*, Analog Devices, One Technol. Way, Norwood, MA, USA, 2013. [Online]. Available: https://www.analog.com/media/en/technical-documentation/data-sheets/ADF4159.pdf

[46] B. Sievert, J. Wittemeier, J. T. Svejda, N. Pohl, D. Erni, and A. Rennings, "Bandwidth-enhanced circularly polarized mm-wave antenna with on-chip ground plane," *IEEE Trans. Antennas Propag.*, vol. 70, no. 10, pp. 9139–9148, Oct. 2022.

[47] J. Wittemeier, M. A. Yildirim, and N. Pohl, "Compact and digitally controlled D-band vector modulator for next-gen radar applications in 130 nm SiGe BiCMOS," *IEEE J. Microw.*, vol. 3, no. 2, pp. 815–826, Apr. 2023.

[48] J. Wittemeier and N. Pohl, "A SiGe-based D-band vector modulator for PMCW radar application," in *Proc. 6th Int. Workshop Mobile Terahertz Syst. (IWMTS)*, Bonn, Germany, 2023, pp. 1–5, doi: 10.1109/IWMTS58186.2023.10207857. [Online]. Available: https://ieeexplore.ieee.org/abstract/document/10207857

[49] J. Bott and N. Pohl, "A multipurpose *D*-band vector modulator for FMCW and PMCW sensing applications in 130 nm SiGe," *IEEE Trans. Microw. Theory Techn.*, vol. 72, no. 8, pp. 4579–4589, Aug. 2024.

[50] H. L. Hartnagel, R. Quay, U. L. Rohde, and M. Rudolph, *Fundamentals of RF and Microwave Techniques and Technologies*. Cham, Switzerland: Springer, 2023.

[51] J. Bott, F. Vogelsang, and N. Pohl, "A D-band phased-array chain based on a tunable branchline coupler and a digitally controlled vector modulator," *IEEE J. Microw.*, vol. 4, no. 1, pp. 101–110, Jan. 2024.

[52] R. K. Mongia and R. Mongia, Eds., *RF and Microwave Coupled-Line Circuits* (Artech House Microwave Library). Boston, MA, USA: Artech House, 2007.

[53] K. Siddiq, M. K. Hobden, S. R. Pennock, and R. J. Watson, "Phase noise in FMCW radar systems," *IEEE Trans. Aerosp. Electron. Syst.*, vol. 55, no. 1, pp. 70–81, Feb. 2019.

[54] T. Krems, W. Haydl, H. Massler, and J. Rudiger, "Millimeter-wave performance of chip interconnections using wire bonding and flip chip," in *IEEE MTT-S Int. Microw. Symp. Dig.*, vol. 1, San Francisco, CA, USA, Jun. 1996, pp. 247–250.

[55] J. Romstadt et al., "A 117.5–155-GHz SiGe × 12 frequency multiplier chain with push-push doublers and a Gilbert cell-based tripler," *IEEE J. Solid-State Circuits*, vol. 58, no. 9, pp. 2430–2440, Sep. 2023.

[56] J. Ding, X. Shang, C. Buck, M. Geen, and N. Ridler, "Low-loss 140–175 GHz MMIC-to-waveguide transitions and MMIC-to-MMIC interconnections," in *Proc. 51st Eur. Microw. Conf. (EuMC)*, London, U.K., Apr. 2022, pp. 91–94.

[57] G. Gramlich, R. Huber, U. Lemmer, and T. Zwick, "Aerosol jet printed millimeter wave interconnects in D-Band," in *Proc. 52nd Eur. Microw. Conf. (EuMC)*, Milan, Italy, Sep. 2022, pp. 298–301.

[58] J. Hebeler, L. Steinweg, and T. Zwick, "Differential bondwire interface for chip-to-chip and chip-to-antenna interconnect above 200 GHz," in *Proc. 52nd Eur. Microw. Conf. (EuMC)*, Milan, Italy, Sep. 2022, pp. 306–309.

[59] P. V. Testa, C. Carta, and F. Ellinger, "Novel high-performance bondwire chip-to-chip interconnections for applications up to 220 GHz," *IEEE Microw. Wireless Compon. Lett.*, vol. 28, no. 2, pp. 102–104, Feb. 2018.

[60] B. Sievert, J. T. Svejda, D. Erni, and A. Rennings, "Spherical mm-wave/THz antenna measurement system," *IEEE Access*, vol. 8, pp. 89680–89691, 2020.

[61] R. E. Collin, *Antennas and Radiowave Propagation* (McGraw-Hill Series in Electrical Engineering). New York, NY, USA: McGraw-Hill, 1985.

[62] D. Bleh, *FMCW MIMO Radar Demonstrator System for 3D Imaging*. Stuttgart, Germany: Fraunhofer Verlag, 2018.

[63] J. Li and P. Stoica, "MIMO radar with colocated antennas," *IEEE Signal Process. Mag.*, vol. 24, no. 5, pp. 106–114, Sep. 2007.

[64] C. A. Balanis, *Antenna Theory*. Hoboken, NJ, USA: Wiley, Apr. 2016.

[65] J. Wittemeier, B. Sievert, M. Dedic, D. Erni, A. Rennings, and N. Pohl, "The impact of group delay dispersion on radar imaging with multiresonant antennas," *IEEE Microw. Wireless Compon. Lett.*, vol. 32, no. 3, pp. 241–244, Mar. 2022.

[66] B. Zhang, G. Xu, R. Zhou, H. Zhang, and W. Hong, "Multi-channel back-projection algorithm for mmWave automotive MIMO SAR imaging with Doppler-division multiplexing," *IEEE J. Sel. Topics Signal Process.*, vol. 17, no. 2, pp. 445–457, Mar. 2023.

[67] T. Jaeschke, C. Bredendiek, and N. Pohl, "A 240 GHz ultra-wideband FMCW radar system with on-chip antennas for high resolution radar imaging," in *IEEE MTT-S Int. Microw. Symp. Dig.*, Seattle, WA, USA, Jun. 2013, pp. 1–4.

[68] T. Jaeschke et al., "3D FMCW SAR imaging based on a 240 GHz SiGe transceiver chip with integrated antennas," in *Proc. German Microw. Conf. (GeMiC)*, Aachen, Germany, Mar. 2014, pp. 1–4.

[69] L. Chen, M. T. Taba, Z. Khalifa, A. Cathelin, and E. Afshari, "A fast back-to-lock DPLL-based 192–210-GHz chirp generator with +5.9-dBm peak output power for sub-THz imaging and sensing," *IEEE J. Solid-State Circuits*, vol. 59, no. 5, pp. 1461–1474, May 2024.

[70] N. Sarmah et al., "A fully integrated 240-GHz direct-conversion quadrature transmitter and receiver chipset in SiGe technology," *IEEE Trans. Microw. Theory Techn.*, vol. 64, no. 2, pp. 562–574, Feb. 2016.

[71] F. Ahmed, M. Furqan, K. Aufinger, and A. Stelzer, "A 240-GHz FMCW radar transceiver with 10 dBm output power using quadrature combining," in *Proc. 15th Eur. Microw. Integr. Circuits Conf. (EuMIC)*, Utrecht, The Netherlands, Jan. 2021, pp. 281–284.

[72] J. Grzyb, K. Statnikov, N. Sarmah, B. Heinemann, and U. R. Pfeiffer, "A 210–270-GHz circularly polarized FMCW radar with a single-lens-coupled SiGe HBT chip," *IEEE Trans. THz Sci. Technol.*, vol. 6, no. 6, pp. 771–783, Nov. 2016.

[73] A. Kaineder, C. Mangiavillano, F. Ahmed, M. Furqan, and A. Stelzer, "240-GHz system on chip FMCW radar for short range applications," in *IEEE MTT-S Int. Microw. Symp. Dig.*, Linz, Austria, Nov. 2020, pp. 1–4.

[74] X. Yi, C. Wang, X. Chen, J. Wang, J. Grajal, and R. Han, "A 220-to-320-GHz FMCW radar in 65-nm CMOS using a frequency-comb architecture," *IEEE J. Solid-State Circuits*, vol. 56, no. 2, pp. 327–339, Feb. 2021.

[75] B. Baccouche et al., "Three-dimensional terahertz imaging with sparse multistatic line arrays," *IEEE J. Sel. Topics Quantum Electron.*, vol. 23, no. 4, pp. 1–11, Jul. 2017.

[76] A. B. Vattulainen, S. Rahman, and D. A. Robertson, "G-band FMCW Doppler radar for close-range environmental sensing," *IEEE Trans. Radar Syst.*, vol. 2, pp. 355–371, Mar. 2024.

[77] F. Vogelsang, D. Starke, J. Wittemeier, H. Rücker, and N. Pohl, "A highly-efficient 120 GHz and 240 GHz signal source in a SiGe-technology," in *Proc. IEEE BiCMOS Compound Semiconductor Integr. Circuits Technol. Symp. (BCICTS)*, Monterey, CA, USA, Nov. 2020, pp. 1–4.

[78] C. Mangiavillano, A. Kaineder, K. Aufinger, and A. Stelzer, "A 1.42-mm$^2$ 0.45–0.49 THz monostatic FMCW radar transceiver in 90-nm SiGe BiCMOS," *IEEE Trans. THz Sci. Technol.*, vol. 12, no. 6, pp. 592–602, Nov. 2022.

[79] D. Starke et al., "A fully integrated 0.48 THz FMCW radar transceiver MMIC in a SiGe-technology," in *Proc. 17th Eur. Microw. Integr. Circuits Conf. (EuMIC)*, Milan, Italy, Sep. 2022, pp. 56–59.

[80] D. Starke et al., "A compact and fully integrated 0.48 THz FMCW radar transceiver combined with a dielectric lens," *Int. J. Microw. Wireless Technol.*, early access, pp. 1–12, 2023, doi: 10.1017/S1759078723001368.

[81] D. Starke et al., "A 360 GHz fully integrated differential signal source with 106.7 GHz continuous tuning range in 90 nm SiGe:C BiCMOS," *IEEE Trans. Microw. Theory Techn.*, vol. 72, no. 8, pp. 4685–4700, Aug. 2024.

[82] J. Bott et al., "A 335–407-GHz SiGe-based subharmonic mixer using a fully integrated LO generation," *IEEE Microw. Wireless Technol. Lett.*, vol. 34, no. 6, pp. 675–678, Jun. 2024.
[83] R. Feger, C. Pfeffer, and A. Stelzer, "A frequency-division MIMO FMCW radar system based on delta–sigma modulated transmitters," *IEEE Trans. Microw. Theory Techn.*, vol. 62, no. 12, pp. 3572–3581, Dec. 2014.
[84] M. Kucharski, A. Ergintav, W. A. Ahmad, M. Krstic, H. J. Ng, and D. Kissinger, "A scalable 79-GHz radar platform based on single-channel transceivers," *IEEE Trans. Microw. Theory Techn.*, vol. 67, no. 9, pp. 3882–3896, Sep. 2019.
[85] D. Zankl, S. Schuster, R. Feger, and A. Stelzer, "What a blast!: A massive MIMO radar system for monitoring the surface in steel industry blast furnaces," *IEEE Microw. Mag.*, vol. 18, no. 6, pp. 52–69, Sep. 2017.
[86] T. Spreng, S. Yuan, V. Valenta, H. Schumacher, U. Siart, and V. Ziegler, "Wideband 120 GHz to 140 GHz MIMO radar: System design and imaging results," in *Proc. Eur. Microw. Conf. (EuMC)*, Paris, France, Sep. 2015, pp. 430–433.
[87] H. J. Ng and D. Kissinger, "Highly miniaturized 120-GHz SIMO and MIMO radar sensor with on-chip folded dipole antennas for range and angular measurements," *IEEE Trans. Microw. Theory Techn.*, vol. 66, no. 6, pp. 2592–2603, Jun. 2018.
[88] W. A. Ahmad et al., "Multimode W-band and D-band MIMO scalable radar platform," *IEEE Trans. Microw. Theory Techn.*, vol. 69, no. 1, pp. 1036–1047, Jan. 2021.
[89] H. J. Ng, M. Kucharski, W. Ahmad, and D. Kissinger, "Multi-purpose fully differential 61- and 122-GHz radar transceivers for scalable MIMO sensor platforms," *IEEE J. Solid-State Circuits*, vol. 52, no. 9, pp. 2242–2255, Sep. 2017.
[90] P. Grüner, M. Klose, and C. Waldschmidt, "A radar system concept for 2D unambiguous angle estimation using widely spaced MMICs with antennas on-chip at 150 GHz," in *IEEE MTT-S Int. Microw. Symp. Dig.*, Los Angeles, CA, USA, Aug. 2020, pp. 1279–1282.
[91] P. Grüner, T. Chaloun, and C. Waldschmidt, "Enhancing angle estimation accuracy of ultra compact two-channel radar MMICs at 160 GHz using a biomimetic antenna array," in *IEEE MTT-S Int. Microw. Symp. Dig.*, Boston, MA, USA, Jun. 2019, pp. 305–308.
[92] A. Dürr, R. Kramer, D. Schwarz, M. Geiger, and C. Waldschmidt, "Calibration-based phase coherence of incoherent and quasi-coherent 160-GHz MIMO radars," *IEEE Trans. Microw. Theory Techn.*, vol. 68, no. 7, pp. 2768–2778, Jul. 2020.
[93] A. Dürr et al., "High-resolution 160-GHz imaging MIMO radar using MMICs with on-chip frequency synthesizers," *IEEE Trans. Microw. Theory Techn.*, vol. 67, no. 9, pp. 3897–3907, Sep. 2019.
[94] M. Jahn, R. Feger, C. Pfeffer, T. F. Meister, and A. Stelzer, "A SiGe-based 140-GHz four-channel radar sensor with digital beamforming capability," in *IEEE MTT-S Int. Microw. Symp. Dig.*, Montreal, QC, Canada, Jun. 2012, pp. 1–3.
[95] A. Visweswaran et al., "A 28-nm-CMOS based 145-GHz FMCW radar: System, circuits, and characterization," *IEEE J. Solid-State Circuits*, vol. 56, no. 7, pp. 1975–1993, Jul. 2021.
[96] H. Papurcu, J. Romstadt, S. Hansen, C. Krebs, K. Aufinger, and N. Pohl, "A wideband four-channel SiGe D-band transceiver MMIC for TDM MIMO FMCW radar," in *Proc. IEEE 23rd Topical Meeting Silicon Monolithic Integr. Circuits RF Syst.*, Las Vegas, NV, USA, Jan. 2023, pp. 12–15.
[97] M. Kahl et al., "SiGe MIMO in-line imager with $12 \times 64$ elements for real-time 3D image acquisition," in *Proc. 48th Int. Conf. Infr., Millim., THz Waves (IRMMW-THz)*, Montreal, QC, Canada, Sep. 2023, pp. 1–2.
[98] E. Turkmen, I. K. Aksoyak, W. Debski, W. Winkler, and A. Ç. Ulusoy, "A 225–265 GHz I-Q receiver in 130-nm SiGe BiCMOS for FMCW radar applications," *IEEE Microw. Wireless Compon. Lett.*, vol. 32, no. 7, pp. 899–902, Jul. 2022.
[99] A. Haimovich, R. Blum, and L. Cimini, "MIMO radar with widely separated antennas," *IEEE Signal Process. Mag.*, vol. 25, no. 1, pp. 116–129, Dec. 2008.
[100] D. Bleh et al., "*W*-band time-domain multiplexing FMCW MIMO radar for far-field 3-D imaging," *IEEE Trans. Microw. Theory Techn.*, vol. 65, no. 9, pp. 3474–3484, Sep. 2017.
[101] T. Bryllert, V. Drakinskiy, K. B. Cooper, and J. Stake, "Integrated 200–240-GHz FMCW radar transceiver module," *IEEE Trans. Microw. Theory Techn.*, vol. 61, no. 10, pp. 3808–3815, Oct. 2013.
[102] R. Dahlbäck, T. Bryllert, G. Granström, M. Ferndahl, V. Drakinskiy, and J. Stake, "Compact 340 GHz homodyne transceiver modules for FMWC imaging radar arrays," in *IEEE MTT-S Int. Microw. Symp. Dig.*, San Francisco, CA, USA, May 2016, pp. 1–4.
[103] D. Wang et al., "240-GHz four-channel power-tuning heterodyne sensing readout system with reflection and transmission measurements in a 130-nm SiGe BiCMOS technology," *IEEE Trans. Microw. Theory Techn.*, vol. 67, no. 12, pp. 5296–5306, Dec. 2019.
[104] I. Abdo et al., "A bi-directional 300-GHz-band phased-array transceiver in 65-nm CMOS with outphasing transmitting mode and LO emission cancellation," *IEEE J. Solid-State Circuits*, vol. 57, no. 8, pp. 2292–2308, Aug. 2022.

**Jonathan Bott** (Graduate Student Member, IEEE) was born in Lünen, Germany. He received the B.Sc. and M.Sc. degrees in electrical engineering and information technology from TU Dortmund University, Dortmund, Germany, in 2014 and 2016, respectively.

From 2016 to 2017, he worked in the automotive industry as a Software Developer. Since 2017, he has been a Research Assistant at the Institute of Integrated Systems, Ruhr University Bochum, Bochum, Germany. His research interests include millimeter-wave (mm-wave) radar system design, circuit and monolithic microwave integrated circuit (MMIC) design using silicon–germanium, and multiple-input–multiple-output (MIMO) direction-of-arrival (DoA) and imaging algorithms.

**Muhammed Ali Yildirim** (Graduate Student Member, IEEE) was born in Essen, Germany. He received the B.Sc. and M.Sc. degrees in electrical engineering and information technology from Ruhr University Bochum, Bochum, Germany, in 2019 and 2022, respectively.

Since 2022, he has been working as a Research Assistant at the Institute of Integrated Systems, Ruhr University Bochum. His current research interests include millimeter-wave (mm-wave) radar and monolithic microwave integrated circuit (MMIC) design using silicon–germanium.

**Benedikt Sievert** (Member, IEEE) was born in Krefeld, Germany. He received the B.Sc., M.Sc., and Dr.-Ing. degrees in electrical engineering from the University of Duisburg-Essen, Duisburg, Germany, in 2017, 2019, and 2023, respectively.

From 2017 to 2023, he was a member of the Laboratory of General and Theoretical Electrical Engineering, University of Duisburg-Essen. In 2024, he joined the Department of Integrated Circuits, Fraunhofer Institute for High Frequency Physics and Radar Techniques (FHR), Wachtberg, Germany. His research interests include integrated circuits and on-chip antennas for millimeter-wave (mm-wave) systems, and theoretical and computational electromagnetics.

**Florian Vogelsang** (Graduate Student Member, IEEE) was born in Hattingen, Germany, in 1993. He received the B.Sc. and M.Sc. degrees in electrical engineering and information technology from Ruhr University Bochum, Bochum, Germany, in 2015 and 2017, respectively.

He has been a Research Assistant with the Institute of Integrated Systems, Ruhr University Bochum, since 2018. His current research interests include wideband radar systems in the millimeter-wave (mm-wave) and terahertz (THz) range, realized as monolithic microwave integrated circuits (MMICs) in silicon–germanium technologies.

**Tobias Welling** was born in Essen, Germany. He received the B.Sc. and M.Sc. degrees in electrical engineering and information technology from Ruhr University Bochum, Bochum, Germany, in 2019 and 2024, respectively, where he is currently pursuing the Ph.D. degree with German TopIng Program and the Institute of Integrated Systems.

His current research interests include system design for *D*-band radar sensors and integrated circuits for millimeter-wave (mm-wave) applications.

Mr. Welling received the ESCRYPT Young Talent Award and the Krohne Award for one of the best bachelor's degrees in information technology in 2020.

**Philipp Konze** was born in Hilden, Germany. He received the B.Sc. degree in electrical engineering and information technology from Ruhr University Bochum, Bochum, Germany, in 2021, where he is currently pursuing the M.Sc. degree.

He is working as a Student Assistant at the Institute of Integrated Systems, Ruhr University Bochum. His research interests include multiple-input–multiple-output (MIMO) radar system simulation, embedded software, and phase-locked loop (PLL) design.

**Daniel Erni** (Member, IEEE) received the Diploma degree in electrical engineering from the University of Applied Sciences Rapperswil (OST), Rapperswil-Jona, Switzerland, in 1986, and the Diploma degree in electrical engineering and the Ph.D. degree in laser physics from ETH Zürich, Zürich, Switzerland, in 1990 and 1996, respectively.

Since 1990, he has been with the Laboratory for Electromagnetic Fields and Microwave Electronics (IFH), ETH Zürich. From 1995 to 2006, he was the Founder and the Head of the Communication Photonics Group, ETH Zürich. Since October 2006, he has been a Full Professor with the Department of General and Theoretical Electrical Engineering, University of Duisburg-Essen, Duisburg, Germany. From 2017 to 2018, he was with the Institute of Electromagnetic Fields (IEF), ETH Zürich, as a Visiting Professor. He is currently a member of the Center for Nanointegration Duisburg-Essen (CENIDE), University of Duisburg-Essen. He is also the Co-Founder of the spin-off company airCode, Duisburg, working on flexible printed radio-frequency identification (RFID) technology. His current research interests include optical interconnects, nanophotonics, plasmonics, ultrasensitive optical biosensing, advanced solar cell concepts, optical and electromagnetic metamaterials, RF, millimeter-wave (mm-wave) and terahertz (THz) engineering, chipless flexible RFIDs, biomedical engineering, bio-electromagnetics, marine electromagnetics, computational electromagnetics, multiscale and multiphysics modeling, numerical structural optimization, and science and technology studies (STSs).

Dr. Erni is a fellow of the Electromagnetics Academy. He is also a member of Materials Chain, the Flagship Program of the University Alliance Ruhr, Electrosuisse, the Swiss Physical Society (SPS), German Physical Society (DPG), and the Optical Society of America (Optica).

**Andreas Rennings** (Member, IEEE) received the Dipl.-Ing. and Dr.-Ing. degrees from the University of Duisburg-Essen, Duisburg, Germany, in 2000 and 2008, respectively. He studied electrical engineering at the University of Duisburg-Essen.

He carried out his diploma work during a stay at the University of California at Los Angeles, Los Angeles, CA, USA. From 2006 to 2008 he was with IMST GmbH, Kamp-Lintfort, Germany, where he worked as an RF Engineer. Since 2008, he has been a Senior Scientist and a Principal Investigator with the Laboratory for General and Theoretical Electrical Engineering, University of Duisburg-Essen. His general research interests include all aspects of theoretical and applied electromagnetics, currently with a focus on medical applications and on-chip millimeter-wave/terahertz (THz) antennas.

Dr. Rennings has received several awards, including the Student Paper Price at the 2005 IEEE Antennas and Propagation Society International Symposium and the Verband der Elektrotechnik Elektronik Informationstechnik (VDE)-Promotionspreis 2009 for his dissertation.

**Nils Pohl** (Senior Member, IEEE) received the Dipl.-Ing. and Dr.Ing. degrees in electrical engineering from Ruhr University Bochum, Bochum, Germany, in 2005 and 2010, respectively.

From 2006 to 2011, he was a Research Assistant with Ruhr University Bochum, where he was involved in integrated circuits for millimeter-wave (mm-wave) radar applications. In 2011, he became an Assistant Professor at Ruhr University Bochum. In 2013, he became the Head of the Department of mm-Wave Radar and High-Frequency Sensors, Fraunhofer Institute for High Frequency Physics and Radar Techniques, Wachtberg, Germany. In 2016, he became a Full Professor of integrated systems at Ruhr University Bochum. He has authored or co-authored more than 200 scientific articles and has issued several patents. His current research interests include ultrawideband mm-wave radar, design, and optimization of mm-wave integrated silicon–germanium (SiGe) circuits and system concepts with frequencies up to 300 GHz and above, and frequency synthesis and antennas.

Prof. Pohl is a member of Verband der Elektrotechnik Elektronik Informationstechnik (VDE), Informationstechnische Gesellschaft (ITG), European Microwave Association (EUMA), and International Union of Radio Science (URSI). He received the Karl-Arnold Award of the North Rhine-Westphalian Academy of Sciences, Humanities and the Arts in 2013 and the IEEE MTT Outstanding Young Engineer Award in 2018. He was a co-recipient of the 2009 EEEfCom Innovation Award, the 2012 European Microwave Integrated Circuits Conference (EuMIC) Prize, the 2015 Best Demo Award of the IEEE Radio Wireless Week, the Best Paper Award at EUMIC 2012, the Best Demo Award at Radio & Wireless Week (RWW) 2015, and the Best Student Paper Awards at Radar Conference (RadarConf) 2020, RWW 2021, and EuMIC 2022.